# Evidence of Plasticity-Driven Conductivity Drop in an Ultra-Low-k Dielectric Organosilicate Glass

Morgan Rusinowicz, Fabien Volpi, Guillaume Parry, Muriel Braccini, Chaymaa Boujrouf, Marc Verdier

# Evidence of Plasticity-Driven Conductivity Drop in an Ultra-Low-k Dielectric Organosilicate Glass

*Morgan Rusinowicz*, Fabien Volpi, Guillaume Parry, Muriel Braccini, Chaymaa Boujrouf and Marc Verdier*

M. Rusinowicz, F. Volpi, G. Parry, M. Braccini, C. Boujrouf, M. Verdier
Univ. Grenoble Alpes, CNRS, Grenoble INP
SIMaP laboratory, 1130 Rue de la Piscine
Saint-Martin-d'Hères 38402, France
E-mail: morgan.rusinowicz@grenoble-inp.fr

Keywords: organosilicate glasses, electrical-mechanical coupling effects, Poole-Frenkel conductions, electrical-nanoindentation tests, finite element method simulations.

Advanced devices (for microelectronics, energy storage, power sourcing,…) are complex architectures of metals and dielectrics subjected to harsh mechanical stresses. The functional reliability of the embedded dielectrics is driven by their ability to preserve their electrical properties (leakage, breakdown,...). Accordingly, understanding the interplay between the mechanical and electrical behaviors of dielectric films is critical to predict the lifetime of functional devices. In this study, the effect of plastic deformation on the electrical conduction of an ultra-low-k dielectric film is elucidated by combining in situ advanced experiments and finite element modeling. Experimentally, "electrical-nanoindentation" tests emphasize the strong correlation between electrical and mechanical failures (leakage degradation, breakdown, plasticity, cracking,…). These experiments also reveal a counterintuitive electrical conduction drop under high mechanical stresses. This phenomenon is reproduced numerically by correcting the Poole-Frenkel conduction law with a strain-dependent factor, and described analytically in terms of space-charge build-up induced by the trapping of holes at the mechanically-generated defects. A threshold strain is identified as the keystone relating this strain-dependent conduction to the current line distribution within the dielectric. This work provides a new understanding of the mechanical/electrical couplings in dielectrics, which opens promising insights into reliability issues for advanced devices.

## 1. Introduction

For more than six decades, the semiconductor industry has extensively developed and integrated innovative materials capable of meeting challenging technical requirements for the fabrication of integrated circuits. These requirements have imposed cross-related conditions on both functional (electrical conduction or insulation, thermal conduction or insulation, transparency or opacity, thermodynamic stability, etc.) and structural properties (stiffness, hardness, toughness, etc.). These material-based improvements have applied concomitantly to the active devices fabricated directly on semiconducting substrates (transistors, diodes, sensors, etc.) and to the upper interconnect structure that allows these devices to communicate with each other. This interconnect structure is a complex architecture of metal lines surrounded by a composite dielectric matrix. However, as the dimensions of devices have shrunk, these interconnect metal lines have moved closer, thus increasing the intrinsic delay of signal propagation within the structure.[1–4] After the replacement of aluminum by copper, which reduced overall interconnect resistance, major improvements in the performance of these interconnects have involved upgrading the dielectric material, which has evolved continuously from dense $SiO_2$ to nanoporous organosilicate glasses (OSG).[5–7,3,8,9,4,10] The driving force for this evolution in dielectric material was to decrease its permittivity *k*, in order to reduce capacitive coupling between the metal lines. In terms of chemistry, this lowering of permittivity was driven by the Clausius-Mosotti relation: it was first obtained by partially replacing highly-polar Si-O bonds by Si-C bonds (methyl groups were then introduced into the $SiO_2$ backbone), thus leading to dense SiOCH low-k dielectrics. Further lowering of permittivity was achieved by introducing nanoporosity (obtained by UV curing after the incorporation of organic porogens), thus leading to nanoporous SiOCH ultra-low-k dielectrics.[11–13] However, these performance improvements were accompanied by a drastic decline in reliability.[2]

From the mechanical point of view, modifications in SiOCH chemistry and density lowered its effective Young's modulus, hardness and toughness,[14–21,10] thus reducing the ability of such structures to sustain mechanical stresses during processing or operation.[22–27] The mechanical properties of low-k dielectrics were essentially measured on full-sheet specimens by bulge testing or by nanoindentation.[15,16,28,19,29]

From the electrical point of view, the introduction of porosity and organic groups led to a dramatic increase in current leakages,[30–32] and dielectric breakdowns have become the most important failure mechanisms in interconnects.[33–39]

The strong interplay between SiOCH chemistry and electrical failures has been extensively studied,[40,41,35,42–44,36] including the effect of metallic contamination.[45,46] In comparison, the interplay between mechanical stresses and electrical failures has been more rarely addressed. Most attempts have focused on the effect of mechanical stresses on the dielectric breakdown of ultra-thin oxide films,[47–50] demonstrating the synergistic effect of mechanical and electrical stresses on bond breaking. Conversely, it has been reported that electrical current initiates mechanical delamination.[51,52] More recently, the effect of mechanical stresses on trap-assisted conduction mechanisms has been studied: within the reversible domain, it has been shown that mechanical stresses lower/increase the trap energy barrier reversibly when tensile/compressive, respectively.[53,54] The latter trend has been shown to depend strongly on the chemistry of the dielectric material.[55] Despite all these studies, a thorough understanding of the effect of mechanical damages on the electrical conduction of ultra-low-k dielectrics still seems to be lacking. Yet this point is crucial for the modeling of time-dependent dielectric breakdown (TDDB) phenomena and for the prediction of device lifetime.[46,56–58,35]

In the present work, a nanoporous SiOCH film deposited on silicon substrate was nanoindented with a home-developed device able to monitor simultaneously and continuously both the electrical and mechanical responses of the film during indentation.[59–61] Nanoindentation is a well-established technique dedicated to the local mechanical testing of materials at nanoscales,[62,63] and is well suited for thin film characterizations.[64,65] The coupling of this technique with electrical measurements allows the analysis of the mechanical and electrical behaviors of thin film materials as well as their interaction. In this study, such “electrical-nanoindentation” tests (performed under biases ranging from 1 to 120 V) enabled to monitor the leakage current from the earliest stages (at the fA level) up to film failure (dielectric breakdown or film cracking). Different mechanical/electrical regimes were observed and could be explained thanks to post mortem analysis and numerical modeling. In particular, a correction to the original Poole-Frenkel law is proposed to account for the film plasticity that occurs continuously during indentation, thus leading to a full description of the evolution of the electrical conductivity. A physical interpretation of this strain-dependent correction is given in terms of plasticity-induced space-charge. This case study of electrical/mechanical experimental monitoring and numerical modeling paves the way to identifying correlations between structural and functional properties that would otherwise be inaccessible.

## 2. Results and Discussion

### 2.1. Electrical-nanoindentation experiments: overall description

**Figure 1** reports a typical set of electrical-nanoindentation tests performed on the SiOCH/Si stack with a Berkovich tip under different voltages (from 1 to 100 V). For these tests, the maximum load was set to 45 mN, leading to typical penetration depths $h$ of 700 nm. A schematic of the experiment defining the relevant dimensions is shown in Figure 1a. The lower part of Figure 1b reports the loading curves (load vs penetration depth) and the upper part reports the evolution of current flowing through the dielectric during indentation. For these experiments, the ammeter was set to "current autorange" mode in order to allow the current to rise to compliance if needed (100 nA). During indentation, both the contact area $A_c$ and the electric field $\boldsymbol{F}$ continuously increase: $A_c$ increases because of the pyramidal shape of the tip but the case of $\boldsymbol{F}$ is slightly more complex. For a given penetration depth, $\boldsymbol{F}$ gradually decays along the tip radius (from the apex to the edge), but its maximum is always located at the tip apex, where it strengthens during indentation because of the decrease in distance $d$. One can define the initial electric field $F_0$ as the electric field at the tip apex when indentation starts. Thus, $F_0$ is the ratio between the applied voltage and the film thickness.

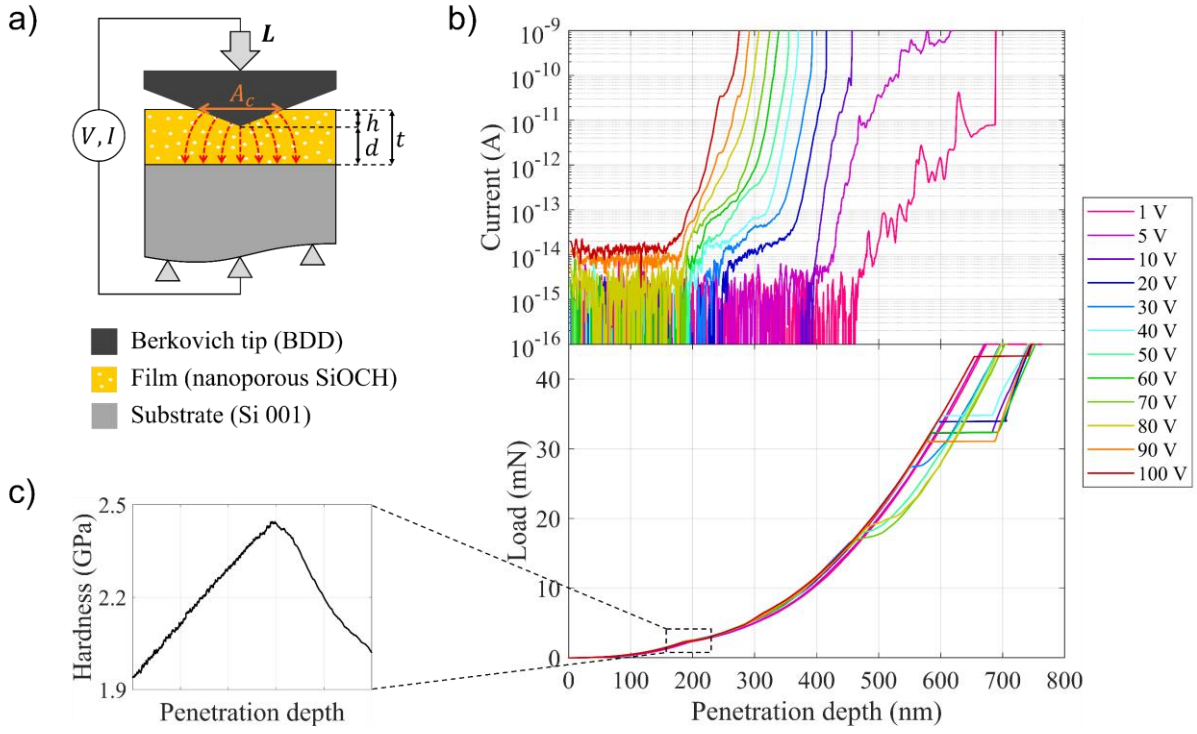


**Figure 1.** a) Schematic of the electrical-nanoindentation experiments. The dotted red arrows represent the current lines, $\boldsymbol{L}$ is the applied mechanical load, $h$ is the penetration depth of the tip into the material, $A_c$ is the contact area, $d$ is the distance between the tip apex and the

substrate during indentation, and *t* is the initial thickness of the pristine film, 330 nm. b) Upper curves: raw current-depth curves (before withdrawal of the open-circuit current) with the current scale cut off at 1 nA (i.e. before 100 nA compliance). Lower curves: corresponding load-depth curves. c) Example of a hardness-depth curve on the first pop-in. Each electrical-nanoindentation curve represents a set of 5 tests.

### 2.2. Mechanical behavior and film damaging

From the mechanical point of view, two distinct stages can be identified on the loading curves:

- Stage 1. From 0 to ~ 190 nm (~ 55% of the film thickness), the loading curves are highly reproducible and follow a given curvature up to a slope change circa 190 nm. This curvature change (usually referred to as a "pop-in" feature) is the signature of a non-reversible mechanical event (brittle cracking, dislocation bursts, phase transformations, etc.[66,67]). This pop-in is clearly observed on the hardness curves, where hardness drops sharply at pop-in (see Figure 1c). The onset of this pop-in is highly reproducible from test to test.
- Stage 2. From ~ 190 nm to the final load, continuous loading with a lower power-law dependence is observed. This second stage is finally marked out by a second pop-in of much larger amplitude (abrupt tip penetration into the sample) and with more dispersed characteristics (onset depth, amplitude,…).

In order to identify the mechanisms driving these loading curves, dedicated indentations with intermediate final penetration depths were performed (**Figure 2**). The series of tests were stopped: either before the first pop-in (at 50, 100 and 150 nm, left), after the first pop-in (at 200 nm, middle) or after the second pop-in (at 500 nm, right). The corresponding loading curves are given in Figure 2a,d,g, the residual imprints of shallow indents observed by AFM are shown in Figure 2b,c, and the residual imprints of deep indents observed by SEM after FIB-slicing in Figure 2e,f,h,j.

Figure 2b,c presents the residual imprints of indents stopped before the first pop-in (50 and 100 nm on Figure 2b, and 150 nm on Figure 2c). The profiles of these imprints were measured by AFM over 2-3 tests for each maximum depth. The residual depths of these imprints are 1-2 nm for the 50 nm indentations, 9-11 nm for the 100 nm indentations, and 25-35 nm for the 150 nm indentations. The existence of these residual imprints after tip removal means that non-reversible deformation of the SiOCH films is initiated at the earliest stages of indentation (at least from 50 nm of penetration depth). This non-reversibility is confirmed by the hysteretic behavior of the loading/unloading curves in Figure 2a. In the following, we will refer to this

non-reversibility by the term “plasticity”, which here gives no information on the irreversible deformation mechanism.

Figure 2e,f presents the residual imprints left right after the first pop-in (final penetration depth of 200 nm). The three-pointed star shape of the imprint (enclosed in an area of typically 1 µm radius) shows that the mechanical event responsible for this first pop-in is a crack in the SiOCH film initiated along the indenter edges. This observation is in accordance with the reported data.[14,16,68] Figure 2d magnifies the pop-in feature shown in Figure 1b.

Finally, Figure 2h,i presents the residual imprints after the second pop-in (final penetration depth of 500 nm). These images show spalling of the SiOCH film, as reported in the literature.[64,68,69] It can also be seen that the SiOCH material at the indent center remained trapped by the indenter apex (indicated on Figure 2i). Finally, the underlying Si substrate remained in its elastic domain throughout the test, as no residual plastic deformation is observed.

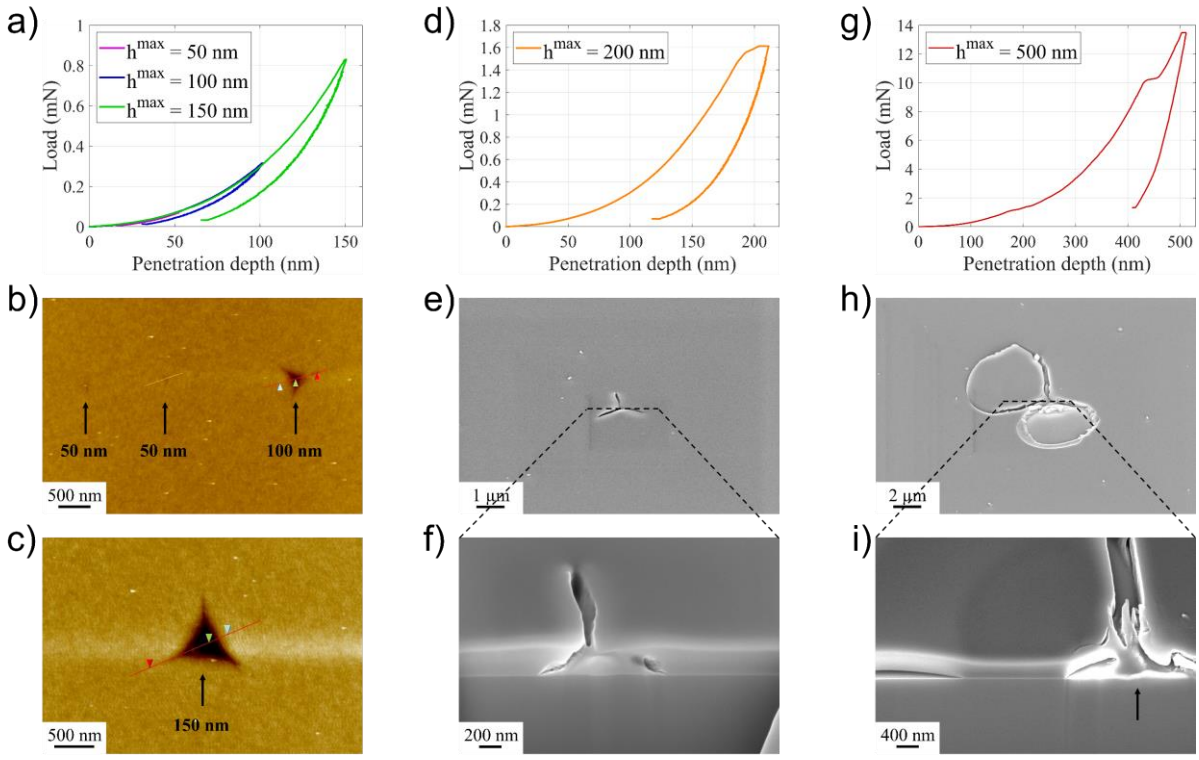


**Figure 2.** a) Load-depth curves for maximum indentation depths of 50, 100 and 150 nm. b) AFM image of the residual indents for indentation depths of 50, 100 nm and c) 150 nm. d) Load-depth curve for a maximum indentation depth of 200 nm. e) SEM image of the residual indent at 200 nm indentation depth viewed from the surface and f) in cross-section after FIB-slicing. g) Load-depth curve for a maximum indentation depth of 500 nm. h) SEM image of the residual indent at 500 nm indentation depth viewed from the surface and i) in cross-section after FIB-slicing. Each loading curve represents a set of 5 tests.

### 2.3. Electrical response

In terms of electrical response, all the current curves of Figure 1b can be described as follows. First, the current remains quite steady at a low base level (in the range of several fA), then it increases continuously over several decades, and it finally undergoes a steep rise. In the initial regime, the steady state current is actually equal to the set-up open-circuit current. In the following analysis, this open-circuit offset will be withdrawn from the raw data. Within this initial regime, the actual leakage current that flows through the SiOCH film is concealed by this base level. This is no longer the case during the second regime, where leakage through the film overtakes this open-circuit base level. It can be clearly seen that the higher the voltage, the earlier the detection of this leakage current. In addition, the apparent slopes gradually increase with the applied voltage: from 3 decades/100 nm to 3 decades/200 nm from 1 to 100 V, respectively. Finally, current reaches the apparatus compliance level (100 nA) shortly after the final steep rise. This "compliance" saturation cannot be seen in the figure as the graph scale is cut at 1 nA in order to emphasize the low-level signals.

### 2.4. Correlation between mechanical damage and electrical leakage

In order to finely distinguish the onset of electrical and mechanical failures at the earliest indentation stages, another set of experiments was performed with the ammeter in a "fixed current range" mode (from 1 to 1000 fA, depending on the test conditions). Under such conditions, current cannot be explored up to the compliance level (it is only limited by the current range) but the signal-to-noise ratio is improved by one order of magnitude. Voltages between 1 and 120 V were applied in steps of 5 V. Each indent, at fixed voltage, was repeated 3 times to ensure good reproducibility. In each test, the open-circuit current was measured before the tip reached the sample surface and was subtracted from the current measured during indentation. Current curves were finally smoothed by a moving average over 300 points (i.e. about 20 nm of penetration depth).

As an illustration, **Figure 3** reports the current-depth and load-depth curves for indentations performed under 5 V (Figure 3a) and 70 V (Figure 3b). As already discussed, both the mechanical and electrical responses display sharp changes on their related curves: a pop-in feature on the mechanical curve and a significant current rise on the electrical curve. Consequently, two critical depths can be defined:

- Critical mechanical depth $h_C^{Mech}$. This critical depth corresponds to the first pop-in depth, i.e. to the onset of mechanical failure of the film. $h_C^{Mech}$ is highly reproducible from test to test and equals ~ 190 nm. For the sake of precision, $h_C^{Mech}$ was extracted at the hardness peak (Figure 1c).
- Critical electrical depth $h_C^{Elec}$. This critical depth corresponds to the depth from which leakage current overtakes the base level. $h_C^{Elec}$ depends strongly on the applied voltage as shown in Figure 3, where $h_C^{Elec}$ ~ 285 nm under 5 V (i.e. greater than $h_C^{Mech}$), while $h_C^{Elec}$ ~ 110 nm under 70 V (i.e. lower than $h_C^{Mech}$).

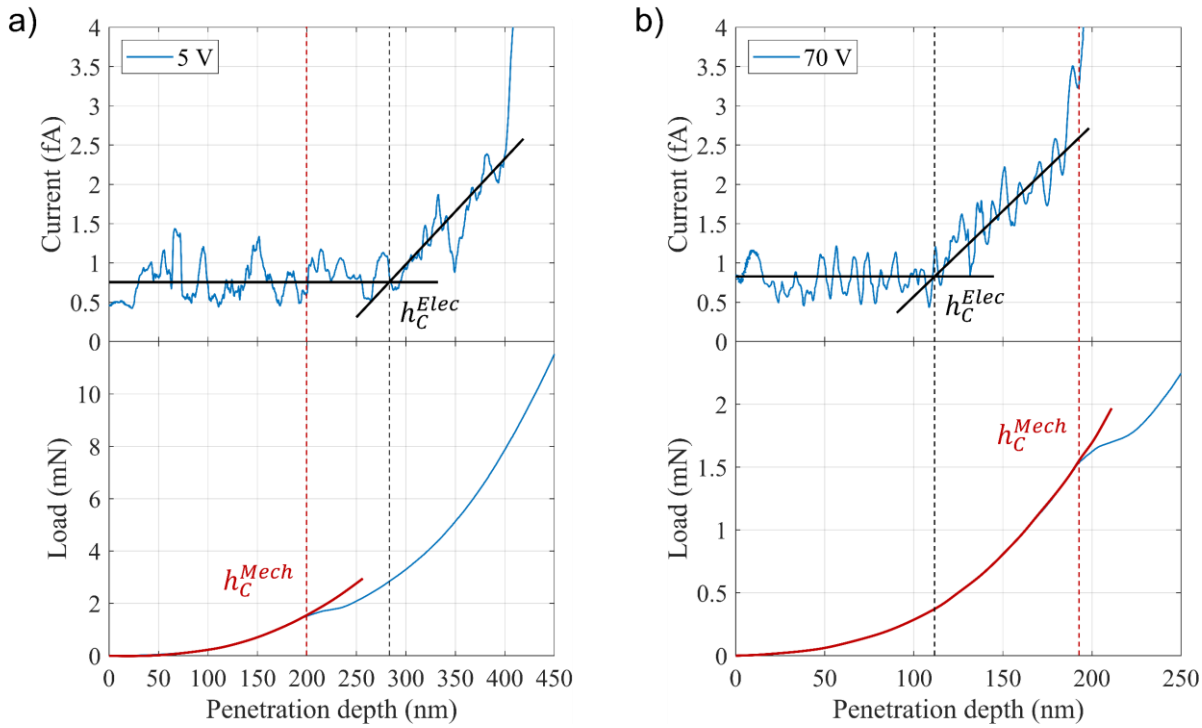


**Figure 3.** Changes in current and load versus penetration depth a) for a voltage of 5 V (case where $h_C^{Elec} > h_C^{Mech}$) and b) for a voltage of 70 V (case where $h_C^{Elec} < h_C^{Mech}$).

After extraction of $h_C^{Elec}$ and $h_C^{Mech}$ for each indentation test (i.e. for each voltage), their difference $h_C^{Elec} - h_C^{Mech}$ can be plotted against the applied voltage (**Figure 4**). With this representation, leakage onset and mechanical failure can be related to the electric field applied. Four cases can be identified (described below from small to large voltages).

- From 1 to 10 V: $h_C^{Elec} > h_C^{Mech}$. With low voltages, current leakage through the dielectric is detected after the film cracking along the tip edges (Figure 2e). It can be noted that the higher

the applied voltage, the earlier the leakage current is detected, which is consistent with an increase in leakage currents under larger electric fields.

- From 10 to 50 V: $h_C^{Elec} = h_C^{Mech}$. In this voltage range, a zero-dwell is observed: film cracking actually triggers leakage currents through the dielectric. This leakage triggering can be attributed to the multiplication of electrical traps that form conduction paths along the crack side-walls.
- From 50 to 90 V: $h_C^{Elec} < h_C^{Mech}$. In this voltage range, leakage current through the SiOCH film is detected before the first pop-in occurs. As in the low voltage range, the higher the applied voltage, the earlier the onset of leakage. Furthermore, two different curvatures can be observed, with a slope change occurring at 75 V. This point will be fully explained in section 2.9 in terms of damage and current line distributions in the SiOCH film.
- From 90 to 120 V: $h_C^{Elec} = 0$. In this high voltage range, leakage current through the SiOCH film is detectable as soon as tip/sample contact is established. As both $h_C^{Elec}$ and $h_C^{Mech}$ are constant in this case, their difference is also constant and equal to ~ -190 nm. This range is of particular interest as it can be used to drive a detailed description of the electrical conduction regime (large analyzable indentation range, no mechanical instability such as film cracking, etc.). The following description of electrical conduction analyses this voltage range, even though the results will explain Figure 4 as a whole.

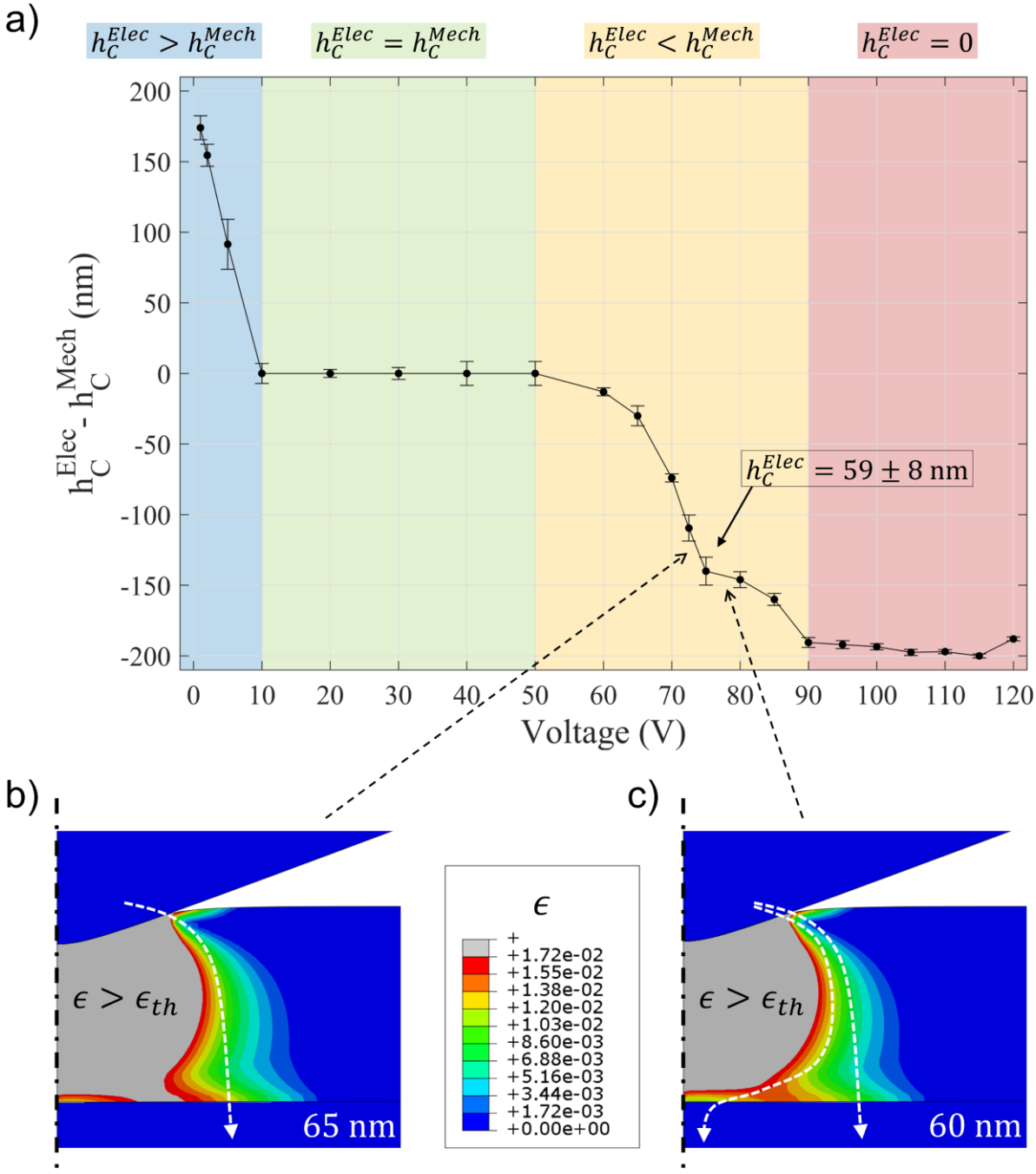


**Figure 4.** a) Difference between electrical and mechanical critical depths versus the applied voltage. Each point is the average over three tests carried out for each voltage, and error bars are calculated by standard deviation on these three values. b) Snapshot at 65 nm depth of the maximum principal plastic strain in the film, thresholded so that the gray area corresponds to the area where strain exceeds the threshold strain $\epsilon_{th}$. Current lines (white dashed arrow) follow a unique path. c) Snapshot at 60 nm depth of the maximum principal plastic strain in the film, thresholded so that the gray area corresponds to the area where strain exceeds the threshold strain $\epsilon_{th}$. Current lines (white dashed arrows) follow two possible paths.

### 2.5. Electrical conduction behavior at high electric fields

**Figure 5** reports the current-depth curves obtained by indenting the SiOCH film under voltages between 90 and 115 V. The solid lines are experimental data. In this voltage regime, the initial electric field $F_0$ ranges from 2.6 to 3.5 MV/cm. Data are only represented up to 200 nm, as the response beyond mechanical cracking (circa 190 nm) is of no interest for this analysis. On all the curves, a significant increase in current is observed at the earliest stages (up to 60-70 nm). This trend is consistent with the increase in both the contact area and the electric field. Beyond this stage, current further increases but with a gentler slope, or even saturates at the highest voltages (105-115 V) before decreasing. This behavior is unexpected as both the contact area and electric field carry on increasing during indentation. Finally, beyond 190 nm, the current sharply increases due to film cracking.

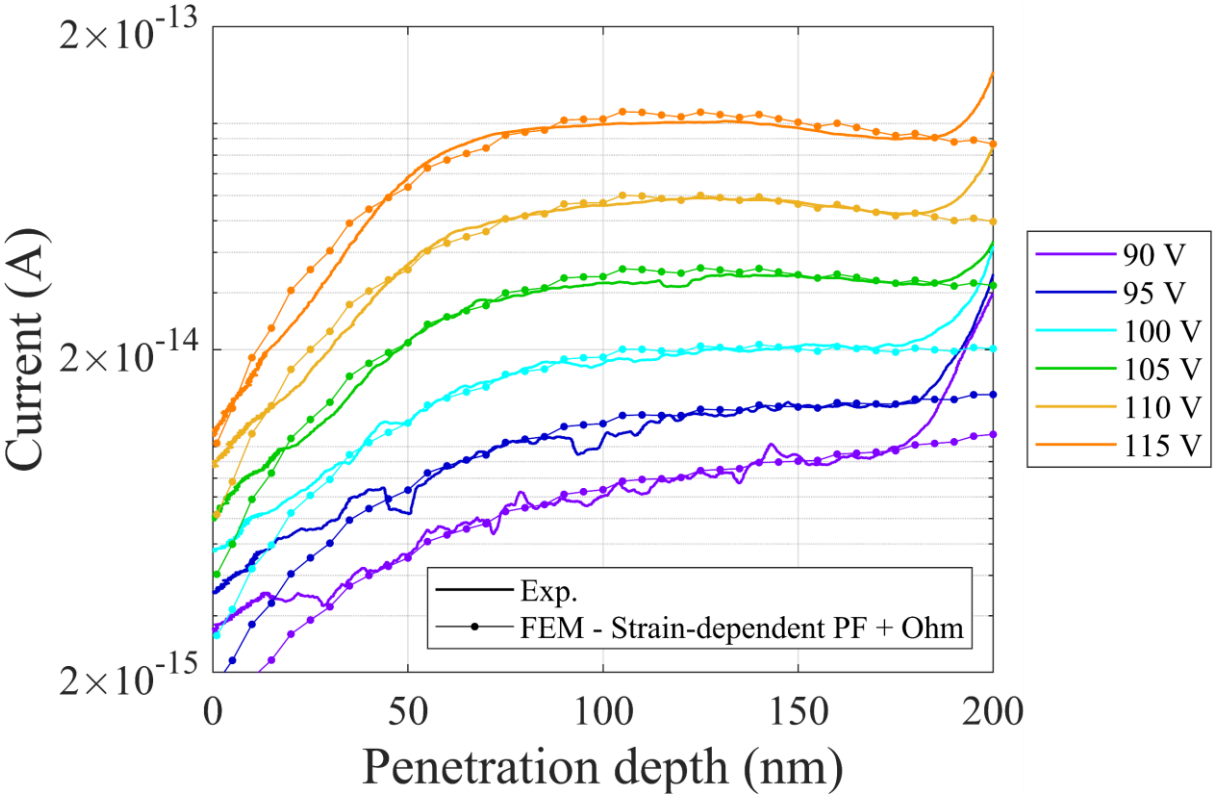


**Figure 5.** Comparison of experimental and numerical current-depth curves, with the model taking into account both strain-dependent Poole-Frenkel and Ohmic conduction, for applied voltages between 90 and 115 V. For each curve, the RMS relative deviation between numerical and experimental data was ~ 5 % over the 30-180 nm range.

### 2.6. Conduction mechanism modeling

Electrical conduction mechanisms in dielectric films have been widely studied in the literature.[70–72] The most widely reported mechanisms for electrical transport in ultra-low-k films are essentially Ohmic, Poole-Frenkel or Schottky conductions depending on the electric field range, the chemistry of the injecting electrode or the dielectric barrier,…[40,73,39] Ohmic conduction is usually observed in low field ranges.[74,52,75] It only depends on the constant carrier density and mobility, leading to a linear relationship between current density and electric field. In contrast, Poole-Frenkel and Schottky conductions are highly non-linear: the emission of free carriers is promoted by the local electric field through the lowering of an energy barrier. In the case of Poole-Frenkel conduction, carriers are emitted from traps in the dielectric bulk, while Schottky conduction is an interface-controlled mechanism. The following analysis will focus on Poole-Frenkel conduction, as it is widely accepted to be the driving mechanism in porous SiOCH films at high electric fields. Poole-Frenkel conduction is described by the following relationship between current density $\boldsymbol{J}$ and electric field $\boldsymbol{F}$ (**Equation 1**).

$$\boldsymbol{J} = C \exp\left(-\frac{\Phi}{r k_B T}\right) \exp\left(\frac{q^{3/2}/\sqrt{\pi \varepsilon_0 k}}{r k_B T} \sqrt{\|\boldsymbol{F}\|}\right) \boldsymbol{F} \qquad (1)$$

In this equation:

- $C$ is a coefficient that depends essentially on the elementary electric charge, the carrier mobility, the effective density of states and the donor-like and/or acceptor-like trap density;
- $\varepsilon_0$, $k_B$, and $T$ are the vacuum permittivity, the Boltzmann constant and the temperature respectively;
- $\Phi$ is the zero-field trap barrier;
- $k$ is the relative dielectric constant;
- $r$ is the compensation factor between 1 and 2;[76–78]
- the second exponential factor represents the lowering of the Poole-Frenkel barrier, expressed as the square-root of the electric field.

This analytical law was implemented in the numerical model presented in the Experimental Section to describe electrical conduction through the SiOCH film. In these numerical simulations, mechanical displacement and voltage are imposed, while mechanical load and electrical current are extracted. The zero-field trap barrier and the dielectric constant values were set to 0.95 eV and 2.5 respectively, in accordance with previous studies.[35] The compensation factor $r$, which must be physically between 1 and 2, was initially set to 1.5. Finally, the $C$ factor was chosen arbitrarily to match the current level at the beginning of

indentation (i.e. before any mechanical/electrical damage). **Figure 6**a compares the experimental and simulated current-depth curves under 115 V (solid line and markers, respectively). It can be observed that the modeled Poole-Frenkel current 1/ increases monotonically throughout indentation, and 2/ increases much faster than the experimental current. Even though this fast current increase is explained by the exponential dependence of current density on electric field (Equation 1), the authors propose that the steep fall in conduction between the experimental data and the standard Poole-Frenkel model is due to mechanical degradation of the SiOCH film. In order to test this hypothesis, the ratio between the experimental and calculated currents (referred to hereafter as "current ratio") was extracted at different depths (from 40 to 160 nm) and then plotted against a "representative strain" $\epsilon_{Rep}$ (Figure 6b). An exponential relationship is clearly observed. The significance of this "representative strain" must now be discussed. During indentation, the film undergoes gradual plastic deformation (Figure 2) described by an extended maximum principal plastic strain field at a given depth. In order to represent this heterogeneous strain field with a simple scalar quantity, the maximum of this mechanical field was extracted from the FEM results and then modulated by a numerical factor, which leads to our "representative strain" (Supporting Information, **Figure S1**).

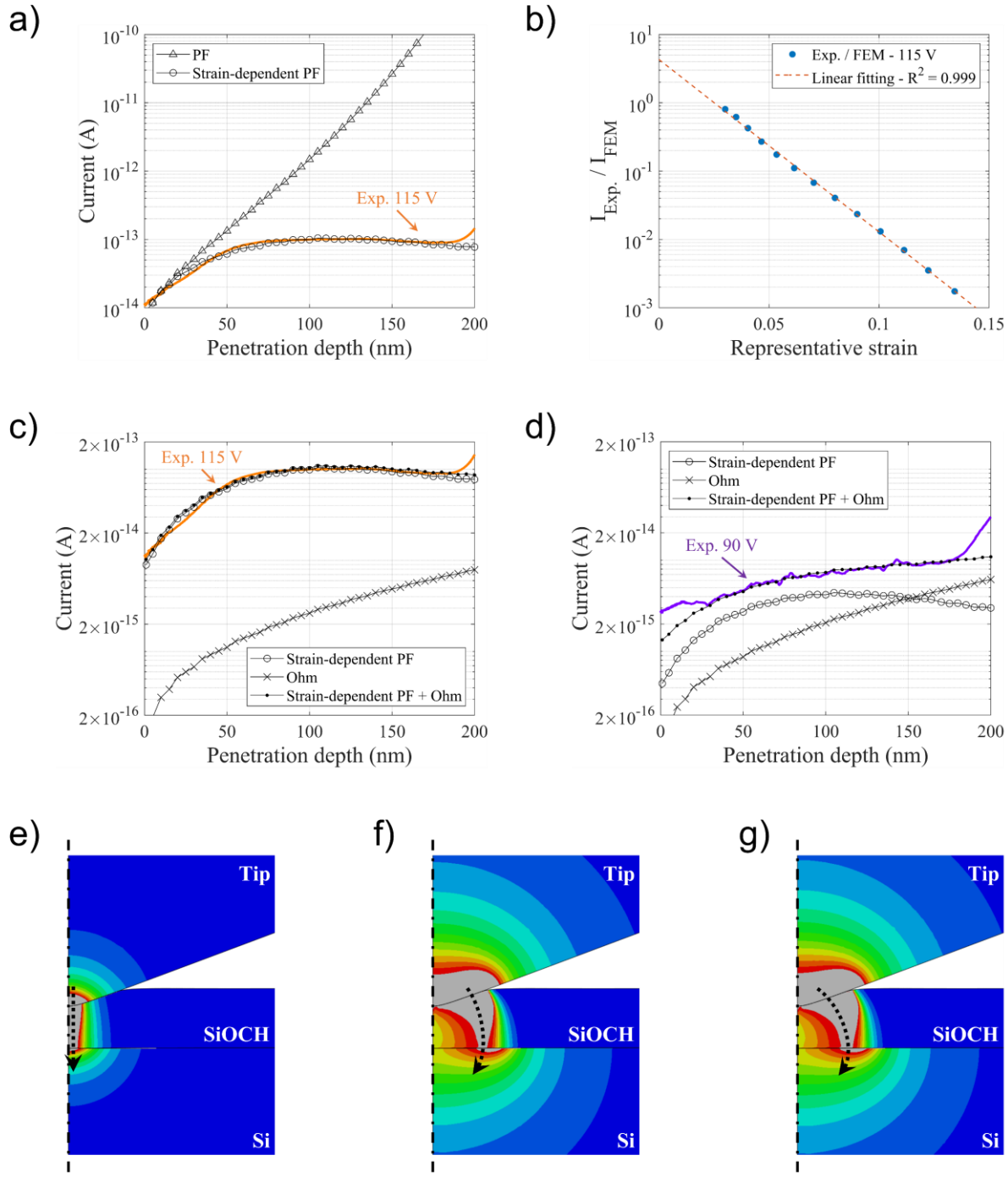


**Figure 6.** a) Comparison of experimental and numerical current-depth curves with the "Poole-Frenkel" and "Strain-dependent Poole-Frenkel" models for an applied voltage of 115 V. b) Linear fitting of the "current ratio" logarithm as a function of the representative strain. c) Comparison of experimental and numerical current-depth curves with the "Strain-dependent Poole-Frenkel", "Ohm" and "Strain-dependent Poole-Frenkel + Ohm" models for an applied voltage of 115 V and d) for an applied voltage of 90 V. e) Current line distribution (shown by the black dashed arrows) at 100 nm indentation depth for the "Poole-Frenkel", f) "Strain-

dependent Poole-Frenkel" and g) "Strain-dependent Poole-Frenkel + Ohm" models. These current density maps are arbitrarily thresholded so that the gray areas are those in which the majority of the current lines flow. On a), c) and d), the RMS relative deviation between numerical and experimental data is ~ 5 % over the 30-180 nm range.

This strong correlation between electrical conduction and mechanical deformation having been identified, a correction of the original Poole-Frenkel law is proposed by the authors (**Equation 2**). It is a threshold constitutive law based on the maximum principal plastic strain $\epsilon$: if this exceeds a threshold strain $\epsilon_{th}$, then the original Poole-Frenkel law is scaled by a decreasing strain exponential $\exp(1 - \epsilon / \epsilon_{th})$. This phenomenological law was implemented in the FEM numerical model. The resulting current curve corresponds to the circular markers denoted "Strain-dependent PF" in Figure 6. The only new adjustable parameter is the threshold strain $\epsilon_{th}$ which reflects the curvature of the current-depth curve. An optimized threshold strain of 0.0172 was obtained, leading to a typical relative deviation between calculation and experiment below 10 %. Such a simple modification of the Poole-Frenkel law reproduces the unexpected current decrease at deep penetrations.

If $\epsilon > \epsilon_{th}$:

$$\boldsymbol{J} = C \exp\left(-\frac{\Phi}{r k_B T}\right) \exp\left(1 - \frac{\epsilon}{\epsilon_{th}}\right) \exp\left(\frac{q^{3/2}/\sqrt{\pi \varepsilon_0 k}}{r k_B T} \sqrt{\|\boldsymbol{F}\|}\right) \boldsymbol{F} \qquad (2)$$

Equation 2 is then introduced in the numerical model where, for a given indentation depth, the strain $\epsilon$ is no longer chosen arbitrarily from the entire strain field, but corresponds to the local strain defined in each element integration point. Moreover, the maximum principal plastic strain field has a notable particularity: it is always in tension (i.e. $\epsilon > 0$), which corresponds to the radial component of the strain tensor in an axisymmetric framework (Supporting Information, **Figure S2)**. This tensile plastic strain is believed to contribute to the breaking of atomic bonds in the material. Those dangling bonds, in turn, will interfere with the conductive mechanism as discussed in the next section. The exact mechanism that produces these dangling bonds (shear or nanopore growth and/or nucleation) cannot be identified at this point. Figure S2 reports the field distributions of the maximum principal plastic strain (responsible for nanopore growth) and of the equivalent plastic strain (shear). Those two field distributions are similar and their levels are close, making it impossible to determine which one prevails. In any case, both approaches allow the same matching of the experimental curves (Figure S2e).

### 2.7. Physical meaning of the strain-dependent Poole-Frenkel correction

The impact of mechanical stress on trap-assisted conduction mechanisms has been rarely explored in the literature. In most studies, applied stresses were kept within their reversible domain, and tensile stresses were found to increase the leakage current (with the notable exception of [79]). The reasons given for this tendency were either the lowering of the trap energy barrier,[53,54] or the change in apparent band gap.[80,81] In contrast, in the present case, the mechanical stress level goes beyond the reversible regime (plasticity is triggered at the earliest stages of indentation) and conduction is seen to decrease when tensile stress increases. The authors propose that the production of structural defects is the origin of this electrical conduction drop.

As already discussed, indentation induces large plastic strains within the dielectric film (Figure 2). In crystalline materials, plastic deformation relies on the gliding of dislocations, while it occurs through the breaking of atomic bonds under shear and/or tensile stresses in amorphous iono-covalent solids.[82–84] From the electrical point of view, these dangling bonds are known to behave as electron/hole traps in dielectrics.[40,53,85,86] These defects are gradually added to the defects already present at low densities.[42,87,80] In the present system, when a positive voltage is applied to the p-type silicon substrate, holes are injected into the SiOCH and flow all through the film up to the grounded p-type diamond tip. As holes travel through the dielectric, some are trapped by these dangling bonds, thus leading to a build-up of the space charge. This current-induced space charge finally modifies the electric field distribution within the SiOCH film.[88] **Figure 7**a presents the band diagram of the Si/SiOCH/C system under a bias of 100 V (Details available in Supporting Information). It was calculated analytically from the integration of Gauss's law with or without space charge, i.e. with or without charged traps (dashed or solid lines, respectively). A trap density $N_T$ of $2\times10^{17}$ $cm^{-3}$ was considered. The introduction of this space charge adds a quadratic contribution to the initially linear hole energy profile. As can be seen in Figure 7b, this quadratic term reduces the slope of the band bending in the vicinity of the Si/SiOCH interface, where holes are injected. This reduction in slope corresponds to the decrease in local electric field. In other words, hole conduction is hampered when trap density increases. This hampering process promotes better conduction along other paths (where trap density is lower) or low-electric field conduction mechanisms (such as Ohmic conduction). We will now focus on the hole-trap interaction energy at atomic scale (Figure 7c). The Poole-Frenkel mechanism relies on the lowering of the effective trap barrier by the local electric field.[89] However, if the local electric field decreases (because of the space charge

effect), barrier lowering also decreases (by an amount $\Delta\Phi_{SC}(N_T)$, indicated in Figure 7c), thus leading to an apparent decay of Poole-Frenkel emission. This trend is in full agreement with Figure 6a: Poole-Frenkel conduction tends to weaken as indentation proceeds. The authors believe that the strain-related scaling factor $\exp(1 - \epsilon / \epsilon_{th})$ introduced in Equation 2 is behind this alteration in conduction. In this equation, if the first two exponentials are merged, the $\epsilon / \epsilon_{th}$ term appears as an apparent increase in the trap barrier, as shown in **Equation 3** and **Equation 4** ($\epsilon > 0$ as strain is tensile).

$$\exp\left(-\frac{\Phi}{rk_BT}\right)\exp\left(1-\frac{\epsilon}{\epsilon_{th}}\right) = \exp\left(1-\frac{\Phi+\Delta\Phi_{Strain}(\epsilon)}{rk_BT}\right) \quad (3)$$

with:

$$\Delta\Phi_{Strain}(\epsilon) = rk_BT\frac{\epsilon}{\epsilon_{th}} \quad (4)$$

It is now important to relate these two approaches: the strain-related scaling factor (with $\Delta\Phi_{Strain}(\epsilon)$ obtained by FEM) and the space-charge-related decay of Poole-Frenkel emission (with $\Delta\Phi_{SC}(N_T)$ obtained by integrating Gauss's law). To do so, the following procedure was applied. First, the "representative strain" $\epsilon_{Rep}$ was extracted from the FEM calculations at every 10 nm of indentation (from 50 to 200 nm). Then it was converted into $\Delta\Phi_{Strain}(\epsilon_{Rep})$ thanks to Equation 4. Additionally, the analytical space charge approach was used to calculate $\Delta\Phi_{SC}(N_T)$ throughout the SiOCH film, and then extracted at a short distance from the Si/SiOCH interface (at the Debye length, where electrical screening fades). Finally, by simple inverse analysis, the trap density $N_T$ required to equalize $\Delta\Phi_{Strain}(\epsilon_{Rep})$ and $\Delta\Phi_{SC}(N_T)$ was extracted by iteration. Consequently, the dependence of trap density $N_T$ on the "representative strain" $\epsilon_{Rep}$ can be plotted (Figure 7d in log-log scale). A simple power-law relationship is clearly observed, with a power exponent $n = 1.75$ (**Equation 5**).

$$N_T \sim \epsilon_{Rep}^{1.75} \quad (5)$$

In terms of defect density, the order of magnitude for $N_T$ falls within the $10^{16}$-$10^{18}$ $cm^{-3}$ range, which is in close agreement with previously reported data for comparable leakages, thus supporting the relevance of the present procedure.[42,43] In our approach, the production of defects by electrical stress was not considered.[90,91,43] Indeed, the electrical stress conditions (charge fluence, current density, electric field,…) in these works were much more severe than in the present work, where the production of defects by mechanical stress should prevail. Finally, this proposed apparent barrier increase with defect density is opposite to the trend observed with the overlap of neighboring potential fields.[74,92] This point is coherent with our

considerations: while these works consider the ability of carriers to hop from full-site to empty-site, we consider the effect of space-charge on the emission barrier.

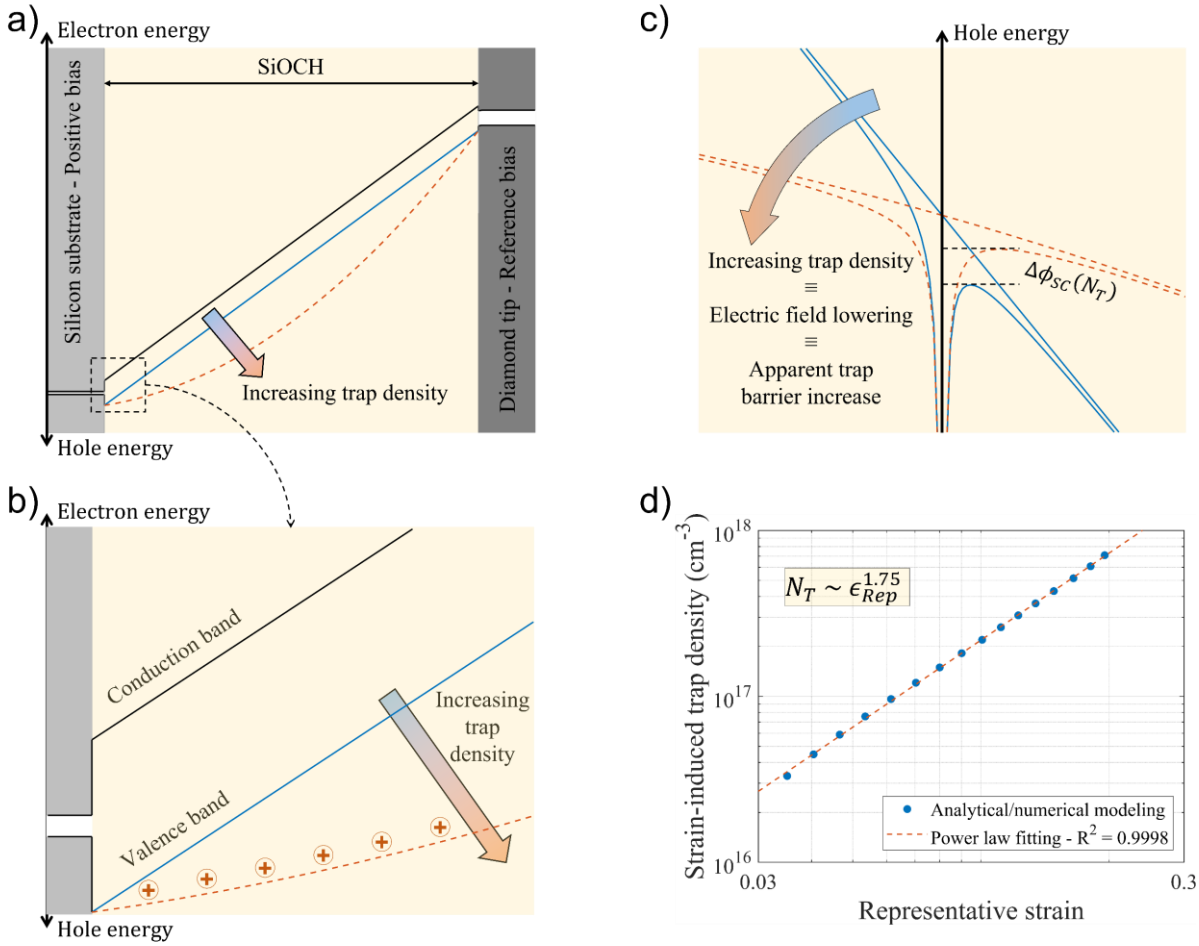


**Figure 7.** a) Band diagram of Si/SiOCH/C system under a bias of 100 V. b) Zoom-in on the band diagram close to the SiOCH/Si interface. c) Hole-trap interaction energy profile. d) Analytically calculated strain-induced trap density versus numerically calculated representative strain.

### 2.8. Additional contribution of Ohmic conduction

As already stated, the space charge that builds up within the dielectric affects the electric charge transport in two ways. First, the current line distribution is forced to change radically during indentation. Although the electric field is initially maximum vertically at the apex of the tip (Figure 6e), it tends to decrease in this axial zone due to the large quantities of defects that are continuously generated. Consequently, Poole-Frenkel conduction progressively drifts away from the contact center to the contact periphery, where defect density is lower (Figure 6f). Secondly, in this axial zone, the decay of the electric field tends to promote low-electric field conduction mechanisms, such as Ohmic conduction for instance. In order to consider this effect,

an Ohmic contribution was implemented in the numerical model (**Equation 6**). The numerical results and experimental data are compared in Figure 6c,d, where only the extreme voltages of this range (115 and 90 V) are shown, for the sake of clarity. As expected, Ohmic conduction affects the overall current more strongly at low voltages (as Ohmic transport prevails where Poole-Frenkel is absent). But it can also be observed that for a given voltage (90 V for instance) this Ohmic contribution has a greater effect on the deep stages when the widely-extended defect distribution hampers Poole-Frenkel conduction. It can be seen in Figure 5 that the proposed model (strain-dependent Poole-Frenkel mechanism and Ohmic contribution) perfectly reproduces the experimental data (scatter markers). The optimized parameters are the following: $C$ = 3.8×10$^{-11}$ S/cm, $r$ = 1.5, $\epsilon_{th}$ = 0.0172, $\sigma_{Ohm}$ = 1.1×10$^{-13}$ S/cm.

If $\epsilon > \epsilon_{th}$:

$$\boldsymbol{J} = C \exp\left(-\frac{\Phi}{r k_B T}\right) \exp\left(1 - \frac{\epsilon}{\epsilon_{th}}\right) \exp\left(\frac{q^{3/2}/\sqrt{\pi \varepsilon_0 k}}{r k_B T} \sqrt{\|\boldsymbol{F}\|}\right) \boldsymbol{F} + \sigma_{Ohm}\, \boldsymbol{F} \qquad (6)$$

This additional Ohmic contribution is further confirmed when considering conduction in the low-field range (below 10V, Figure 4). The numerical extrapolation of these current curves to this low-field range matches the experimental data without any adjustment of the parameters (Supporting Information, **Figure S3**). This point confirms the predominance of Ohmic conduction at low fields.

### 2.9. Relevance of the threshold strain

A final argument that supports the model proposed above is its ability to explain the change in slope in Figure 4 (voltage range between 50 and 90 V, where $h_C^{Elec} < h_C^{Mech}$). The slope change is observed at 75 V, which corresponds to a critical electrical depth $h_C^{Elec}$ of 59 ± 8 nm. If one focusses on the strain field distribution in the SiOCH film (Figure 4b,c), it can be seen that this depth corresponds to the percolation limit for the threshold strain $\epsilon_{th}$: before percolation, Poole-Frenkel conduction can reach the silicon substrate close to the tip apex (red arrows), while it is repelled to the periphery beyond percolation. In the latter case, the apparent resistance of the film is greater than in the former case, thus delaying the onset of large leakage currents.

## 3. Conclusion

In summary, our work provides a comprehensive understanding of the interplay between the mechanical and electrical behaviors of an ultra-low-k dielectric film by both experimental and numerical means. A recently developed technique (electrical-nanoindentation) is first used to correlate the electrical and mechanical failures of an SiOCH film: onset of leakage current, dielectric breakdown, plasticity, film cracking,... Most importantly, electrical-nanoindentation tests reveal a counterintuitive trend: even though both electric field and contact area increase, current is seen to saturate and even decrease during indentation. This unexpected behavior is explained as follows: while indentation proceeds, the plastically-induced defects trap electrical charges (holes), thus causing a space charge to build up within the SiOCH film. This repelling space charge reduces Poole-Frenkel emission by moderating the lowering of barrier energy required for electrical conduction. This mechanism is modeled numerically by correcting the Poole-Frenkel conduction law with a strain-dependent factor. To do so, a threshold strain $\epsilon_{th}$ is introduced into the model: above $\epsilon_{th}$, local Poole-Frenkel conduction is reduced by a factor that decreases exponentially with local plastic strain. Perfect matching of the experimental data over a wide range of electrical and mechanical stresses is thus obtained. A simple analytical model based on Gauss's law is then used to relate the local defect density to plastic strain. Finally, from independent experimental results, this threshold strain is identified as the driving criterion for the change in current line distribution within the dielectric during indentation: $\epsilon_{th}$ appears to be the percolation threshold above which current lines are repelled to the contact periphery. We believe that this case study of electrical/mechanical experimental monitoring and numerical modeling will have great significance in correlations between structural and functional properties that would be unachievable otherwise.

## 4. Experimental Section/Methods

*Sample*: The sample was a simple stack consisting of a thin nanoporous SiOCH film on a (001)-oriented silicon substrate. Nanoporous SiOCH is one of the silicon based ultra-low-k materials and belongs to the organosilicate glasses (OSG). It contains a silica backbone and characteristic Si–$CH_3$ terminating groups.[7,11] Film was deposited by Plasma Enhanced Chemical Vapor Deposition (PECVD) at 225 °C with two precursors and two steps. The first step consisted in co-depositing the SiOCH matrix (diethoxymethylsilane precursor) with a thermally-unstable organic phase called porogen.[93] The second step was dedicated to porogen removal using UV rays,[94,95] leading to a porous material (20-30% of porosity) with a dielectric constant of 2.5. The film was 330 nm-thick. The Si substrate was p-type with a resistivity of 20 Ω cm.

*Electrical-nanoindentation set-up*: The experimental set-up combined various commercial modules with customized adaptations. A more detailed description of the set-up is given in.[60,61] The nanoindentation head was a commercial actuator (InForce 50 actuator from Nanomechanics Inc. / KLA-Tencor) that enabled continuous stiffness measurement (CSM) for hardness and elastic modulus monitoring.[96] All the experiments presented in this paper were performed with boron-doped diamond (BDD) Berkovich tips with resistivity in the range of [0.2-2] Ω cm supplied by Synton-MDP. It was decided to use this reference geometry as it is comparable with most works already reported in the literature, but any other tip geometries can be used (flat-punch, cube-corner or spherical tips). The actuator and samples were displaced with linear positioners from SmarAct GmbH. The whole electrical measurement chain was fully guarded up to the tip, leading to ultra-low set-up leakage (in the fA range). The set-up leakage was measured before each test in an open-circuit configuration, thus the current offset can be annulled by simple subtraction. The set-up shielding resulted in a noise RMS-amplitude of circa 3 fA. Ground planes were used to prevent spurious capacitive couplings. Different electrical magnitudes could be measured with this set-up: leakage current, quasi-static resistance, dielectric capacitance, piezoresponse, etc. In the present case, the focus was on electrical conduction: only currents were monitored. Current measurements were conducted at the tip side with a highly-sensitive ammeter (sub-femtoamp 6430 model from Keithley, with a current sensitivity as low as the fA range with an integration time of 40 ms). Current compliance was set to 100 nA. In this configuration, electrical bias was applied to the sample with a voltage source (6517B model from Keithley), while tip bias was set at ground level.

*Residual imprint characterizations*: Residual nanoindentation imprints were observed by Atomic Force Microscopy (AFM) and Scanning Electron Microscopy (SEM). The AFM apparatus was a NanoObserver AFM from CSI/Scientec, and the SEM apparatus was a Gemini SEM 500 from Carl Zeiss. Cross-views were taken after focused ion-beam (FIB) milling, using a FIB Cross Beam NVision 40 from Carl Zeiss (Ga source with an acceleration voltage of 30 kV and current intensity of 300 pA).

*Finite-element modeling*: Numerical calculations were performed by the Finite Element Method (FEM) using the ABAQUS® commercial software with a model set up in a 2D axisymmetric framework. The overall system consisted of three distinct deformable bodies: a substrate, a 330 nm-thick film fully tied to the substrate, and an indenter whose geometry corresponded to the experimental Berkovich tip profile. From a mechanical point of view, the simulations involved applying a vertical displacement on the upper surface of the tip to bring it into contact with the film surface, while the lower surface of the substrate was embedded. Thus, the stress/strain distribution in the system could be captured. The reaction force could also be extracted, enabling a "load-depth" loading curve to be plotted. The mechanical behavior of the indenter and the substrate was assumed to be isotropic linear elastic and that of the film elastic-plastic. Film plasticity was introduced by a Drucker-Prager law which, in addition to taking into account plastic deformation under shear, can also model the densification of the "real" nanoporous film under the effect of hydrostatic pressure. This type of yield criterion considering the effect of hydrostatic pressure is used to describe the densification of amorphous silica induced by nanoindentation,[97] a material similar to SiOCH in terms of structure. Concerning the electrical aspect, a potential bias was applied between the upper surface of the tip and the lower surface of the substrate throughout the indentation process. Thus, current density and electric field distribution in the system could be captured during the penetration of the tip into the sample. The current flowing through the indenter/film contact surface could also be extracted, and then used to plot "current-depth" electrical curve. The electrical behavior of the indenter and substrate was assumed to be ohmic while that of the film is what we seek to identify in this paper. It can be noted that the results are not sensitive to the electrical constitutive laws and properties of the indenter and the substrate because the film is much more resistive than the materials composing these two systems. In these simulations, the loading was applied incrementally at constant voltage. An implicit scheme was used to solve the mechanical

equilibrium equations simultaneously with the electrical steady state equations. Calculations were performed iteratively using Newton's method and solved with the ABAQUS®/Standard solver. Full details of the modeling process (such as numerical details, methodology used to determine the properties, integration of the constitutive laws) are provided in the Supporting Information, **Figure S4** and **Table S1**.

*Statistical Analysis*: The original sample was a 300 mm large microelectronic-type sample, which was cut into several 1×1 $cm^2$ pieces. The experiments were repeated several times (approximately 3-5 times, depending on the test under consideration) on multiple locations/pieces (~ 3-5 locations/pieces) on 4 different pieces. All raw results were similar, but the fine trends shown in this article could only be discriminated when comparing the results obtained on the same piece during the same experimental run. Comparison of "electrical" curves were only made on tests were the "mechanical" curves were identical. The extraction of the critical electrical and mechanical depths (Figures 3 and 4) were performed from graphical analysis, the reported data are the mean values over at least three tests carried out for each voltage, and error bars are calculated by standard deviation on these three values. The numerical fitting of the electrical curves (Figures 5 and 6) was performed by manual iteration until the maximum relative deviation falls below 10 % for each value of voltage and penetration depth. For each curve, the RMS relative deviation between numerical and experimental data was circa 5 % over the 30-180 nm range.

**Supporting information**

Supporting Information is available from the Wiley Online Library or from the author.

**Acknowledgements**

This work was carried out with the financial support of the Centre of Excellence of Multifunctional Architectured Materials "CEMAM" n° ANR-10-LABX-44-01. The CEMAM program is funded by the French Agence Nationale de la Recherche (ANR).

The authors would like to thank J.C. Royer and D. Fossati from STMicroelectronics for supplying the SiOCH sample, as well as F. Charlot from the CMTC platform (https://cmtc.grenoble-inp.fr) for FIB preparation.

**References**


[1] D. C. Edelstein, G. A. Sai-Halasz, Y. J. Mii, *IBM J. Res. Dev.* **1995**, *39*.
[2] M. Morgen, E. T. Ryan, J.-H. Zhao, C. Hu, T. Cho, P. S. Ho, *Annu. Rev. Mater. Sci.* **2000**, *30*, 645.
[3] D. Shamiryan, T. Abell, F. Iacopi, K. Maex, *Mater. Today* **2004**, *7*, 34.
[4] A. Grill, S. M. Gates, T. E. Ryan, S. V. Nguyen, D. Priyadarshini, *Appl. Phys. Rev.* **2014**, *1*, 011306.
[5] A. Grill, D. A. Neumayer, *J. Appl. Phys.* **2003**, *94*, 6697.
[6] K. Maex, M. R. Baklanov, D. Shamiryan, F. lacopi, S. H. Brongersma, Z. S. Yanovitskaya, *J. Appl. Phys.* **2003**, *93*, 8793.
[7] A. Grill, *J. Appl. Phys.* **2003**, *93*, 1785.
[8] R. J. O. M. Hoofman, G. J. A. M. Verheijden, J. Michelon, F. Iacopi, Y. Travaly, M. R. Baklanov, Zs. Tökei, G. P. Beyer, *Microelectron. Eng.* **2005**, *80*, 337.
[9] B. D. Hatton, K. Landskron, W. J. Hunks, M. R. Bennett, D. Shukaris, D. D. Perovic, G. A. Ozin, *Mater. Today* **2006**, *9*, 22.
[10] X. Gu, H. Deng, Z. Tong, X. Jing, *Jpn. J. Appl. Phys.* **2017**, *56*, 07KF01.
[11] C. A. Yuan, O. van der Sluis, G. Q. Zhang, L. J. Ernst, W. D. van Driel, A. E. Flower, R. B. R. van Silfhout, *Appl. Phys. Lett.* **2008**, *92*, 061909.
[12] M. R. Baklanov, E. A. Smirnov, L. Zhao, *ECS Trans.* **2011**, *35*, 717.
[13] V. Jousseaume, J. El Sabahy, C. Yeromonahos, G. Castellan, A. Bouamrani, F. Ricoul, *Microelectron. Eng.* **2017**, *167*, 69.
[14] J. B. Vella, A. A. Volinsky, I. S. Adhihetty, N. V. Edwards, W. W. Gerberich, *MRS Proc.* **2002**, *716*, B12.13.
[15] A. A. Volinsky, J. B. Vella, W. W. Gerberich, *Thin Solid Films* **2003**, *429*, 201.
[16] R. J. Nay, O. L. Warren, D. Yang, T. J. Wyrobek, *Microelectron. Eng.* **2004**, *75*, 103.
[17] T. K. S. Wong, B. Liu, B. Narayanan, V. Ligatchev, R. Kumar, *Thin Solid Films* **2004**, *462–463*, 156.
[18] S. Takada, N. Hata, Y. Seino, N. Fujii, T. Kikkawa, *J. Appl. Phys.* **2006**, *100*, 123512.
[19] F. Ciaramella, V. Jousseaume, S. Maitrejean, M. Verdier, B. Remiat, A. Zenasni, G. Passemard, *Thin Solid Films* **2006**, *495*, 124.
[20] M. Fujikane, S. Nagao, X. W. Liu, D. Chrobak, A. Lehto, S. Yamanaka, R. Nowak, *J. Alloys Compd.* **2008**, *448*, 293.
[21] V. Jousseaume, G. Rolland, D. Babonneau, J. P. Simon, *Thin Solid Films* **2009**, *517*, 4413.
[22] J. M. Bustillo, R. T. Howe, R. S. Muller, *Proc. IEEE* **1998**, *86*, 1552.
[23] J. W. Evans, J. Y. Evans, P. Lall, S. L. Cornford, *Microelectron. Reliab.* **1998**, *38*, 523.
[24] V. Gonda, J. M. J. Den Toonder, J. Beijer, G. Q. Zhang, W. D. van Driel, R. J. O. M. Hoofman, L. J. Ernst, *Microelectron. Reliab.* **2004**, *44*, 2011.
[25] C. D. Hartfield, E. T. Ogawa, Y.-J. Park, T.-C. Chiu, H. Guo, *IEEE Trans. Device Mater. Reliab.* **2004**, *4*, 129.
[26] T. Tekin, *IEEE J. Sel. Top. Quantum Electron.* **2011**, *17*, 704.
[27] S. Raghavan, I. Schmadlak, G. Leal, S. K. Sitaraman, *Eng. Fract. Mech.* **2016**, *153*, 259.
[28] Y. Xiang, X. Chen, T. Y. Tsui, J.-I. Jang, J. J. Vlassak, *J. Mater. Res.* **2006**, *21*, 386.
[29] Y. Lin, Y. Xiang, T. Y. Tsui, J. J. Vlassak, *Acta Mater.* **2008**, *56*, 4932.
[30] W. Volksen, R. D. Miller, G. Dubois, *Chem. Rev.* **2010**, *110*, 56.
[31] T. K. S. Wong, *Materials* **2012**, *5*, 1602.
[32] J. Borja, J. L. Plawsky, T.-M. Lu, H. Bakhru, W. N. Gill, *J. Appl. Phys.* **2014**, *115*, 084107.
[33] J. R. Lloyd, E. Liniger, T. M. Shaw, *J. Appl. Phys.* **2005**, *98*, 084109.

[34] E. Van Besien, M. Pantouvaki, L. Zhao, D. De Roest, M. R. Baklanov, Z. Tőkei, G. Beyer, *Microelectron. Eng.* **2012**, *92*, 59.
[35] E. Chery, X. Federspiel, D. Roy, F. Volpi, J.-M. Chaix, *Microelectron. Eng.* **2013**, *109*, 90.
[36] Y.-L. Cheng, C.-Y. Lee, W.-J. Hung, G.-S. Chen, J.-S. Fang, *Surf. Coat. Technol.* **2018**, *350*, 57.
[37] S. Peng, H. Zhou, T. Kim, H.-B. Chen, S. X.-D. Tan, *IEEE Trans. Very Large Scale Integr. VLSI Syst.* **2018**, *26*, 239.
[38] E. Y. Wu, *IEEE Trans. Electron Devices* **2019**, *66*, 4523.
[39] J. Palmer, G. W. Zhang, J. R. Weber, C.-Y. Lin, C. Perini, R. Kasim, In *2021 IEEE International Reliability Physics Symposium (IRPS)*, IEEE, Monterey, CA, USA, **2021**, pp. 1–2.
[40] K. Y. Yiang, W. J. Yoo, Q. Guo, A. Krishnamoorthy, *Appl. Phys. Lett.* **2003**, *83*, 524.
[41] H. Miyazaki, D. Kodama, N. Suzumura, *J. Appl. Phys.* **2009**, *106*, 104103.
[42] T. A. Pomorski, B. C. Bittel, P. M. Lenahan, E. Mays, C. Ege, J. Bielefeld, D. Michalak, S. W. King, *J. Appl. Phys.* **2014**, *115*, 234508.
[43] C. Wu, Y. Li, M. R. Baklanov, K. Croes, *ECS J. Solid State Sci. Technol.* **2015**, *4*, N3065.
[44] Z.-J. Ding, Y.-P. Wang, W.-J. Liu, S.-J. Ding, M. R. Baklanov, D. W. Zhang, *J. Phys. Appl. Phys.* **2018**, *51*, 115103.
[45] J. Noguchi, *IEEE Trans. Electron Devices* **2005**, *52*, 1743.
[46] F. Chen, O. Bravo, K. Chanda, P. McLaughlin, T. Sullivan, J. Gill, J. Lloyd, R. Kontra, J. Aitken, In *2006 IEEE International Reliability Physics Symposium Proceedings*, IEEE, San Jose, CA, **2006**, pp. 46–53.
[47] S. Jeffery, C. J. Sofield, J. B. Pethica, *Appl. Phys. Lett.* **1998**, *73*, 172.
[48] T.-C. Yang, K. C. Saraswat, *IEEE Trans. ELECTRON DEVICES* **2000**, *47*, 10.
[49] Y. S. Choi, H. Park, T. Nishida, S. E. Thompson, *J. Appl. Phys.* **2009**, *105*, 044503.
[50] Y.-L. Wu, J.-J. Lin, B.-T. Chen, C.-Y. Huang, *IEEE Trans. Device Mater. Reliab.* **2012**, *12*, 158.
[51] T. Breuer, U. Kerst, C. Boit, E. Langer, H. Ruelke, In *2010 IEEE International Reliability Physics Symposium*, IEEE, Garden Grove (Anaheim), CA, USA, **2010**, pp. 890–894.
[52] T. L. Tan, C. L. Gan, A. Y. Du, Y. C. Tan, C. M. Ng, *J. Mater. Res.* **2008**, *23*, 1802.
[53] Y.-L. Yang, T.-F. Young, T.-C. Chang, F.-Y. Shen, J.-H. Hsu, T.-M. Tsai, K.-C. Chang, H.-L. Chen, *Appl. Phys. Lett.* **2013**, *102*, 192912.
[54] M. T. Alam, K. E. Maletto, J. Bielefeld, S. W. King, M. A. Haque, *Microelectron. Reliab.* **2015**, *55*, 846.
[55] S. Habermehl, R. T. Apodaca, *Appl. Phys. Lett.* **2004**, *84*, 215.
[56] N. Suzumura, S. Yamamoto, D. Kodama, H. Miyazaki, M. Ogasawara, J. Komori, E. Murakami, In *2008 IEEE International Reliability Physics Symposium*, IEEE, Phoenix, AZ, USA, **2008**, pp. 138–143.
[57] S.-C. Lee, A. S. Oates, K.-M. Chang, *IEEE International Reliability Physics Symposium*, **2009**, 481.
[58] K. Croes, C. J. Wilson, M. Lofrano, G. P. Beyer, Z. To, *Microelectron. Eng.* **2011**, 6.
[59] S. Comby-Dassonneville, F. Volpi, M. Verdier, *Sens. Actuators Phys.* **2019**, *294*, 185.
[60] F. Volpi, M. Rusinowicz, S. Comby-Dassonneville, G. Parry, C. Boujrouf, M. Braccini, D. Pellerin, M. Verdier, *Rev. Sci. Instrum.* **2021**, *92*, 035102.
[61] F. Volpi, C. Boujrouf, M. Rusinowicz, S. Comby-Dassonneville, F. Mercier, R. Boichot, M. Chubarov, R. C. Germanicus, F. Charlot, M. Braccini, G. Parry, D. Pellerin, M. Verdier, *Thin Solid Films* **2021**, *735*, 138891.
[62] J. B. Pethica, R. Hutchings, W. C. Oliver, *Philos. Mag. A* **1983**, *48*, 593.
[63] J. L. Loubet, J. M. Georges, O. Marchesini, G. Meille, *J. Tribol.* **1984**, *106*, 43.
[64] S. J. Bull, *J. Phys. Appl. Phys.* **2005**, *38*, R393.

[65] G. Abadias, E. Chason, J. Keckes, M. Sebastiani, G. B. Thompson, E. Barthel, G. L. Doll, C. E. Murray, C. H. Stoessel, L. Martinu, *J. Vac. Sci. Technol. Vac. Surf. Films* **2018**, *36*, 020801.
[66] K. Fu, Y. Tang, L. Chang, In *Fracture Mechanics - Properties, Patterns and Behaviours* (Ed.: Alves, L. M.), InTech, **2016**.
[67] C. A. Schuh, *Mater. Today* **2006**, *9*, 32.
[68] V. N. Sekhar, T. C. Chai, S. Balakumar, L. Shen, S. K. Sinha, A. A. O. Tay, S. W. Yoon, *J. Mater. Sci. Mater. Electron.* **2009**, *20*, 74.
[69] S.-Y. Chang, H.-C. Tsai, J.-Y. Chang, S.-J. Lin, Y.-S. Chang, *Thin Solid Films* **2008**, *516*, 5334.
[70] S. M. Sze, K. K. Ng, *Physics of semiconductor devices*, 3rd ed., Wiley-Interscience, Hoboken, N.J, **2007**.
[71] F.-C. Chiu, *Adv. Mater. Sci. Eng.* **2014**, *2014*, 1.
[72] K. A. Nasyrov, V. A. Gritsenko, *UFN* **2013**, *56*, 999.
[73] V. C. Ngwan, C. Zhu, A. Krishnamoorthy, *Appl. Phys. Lett.* **2004**, *84*, 2316.
[74] W. Vollmann, *Phys. Status Solidi A* **1974**, *22*, 195.
[75] D. Dergez, M. Schneider, A. Bittner, N. Pawlak, U. Schmid, *Thin Solid Films* **2016**, *606*, 7.
[76] J. R. Yeargan, H. L. Taylor, *J. Appl. Phys.* **1968**, *39*, 5600.
[77] R. Ongaro, A. Pillonnet, *Rev. Phys. Appliquée* **1989**, *24*, 1097.
[78] W. R. Harrell, J. Frey, *Thin Solid Films* **1999**, 10.
[79] B. Cheng, L. Xiong, Q. Cai, H. Shi, J. Zhao, X. Su, Y. Xiao, S. Lei, *ACS Appl. Mater. Interfaces* **2016**, *8*, 34648.
[80] X. Guo, H. Zheng, S. W. King, V. V. Afanas'ev, M. R. Baklanov, J.-F. de Marneffe, Y. Nishi, J. L. Shohet, *Appl. Phys. Lett.* **2015**, *107*, 082903.
[81] A. Kruv, B. Kaczer, A. Grill, M. Gonzalez, J. Franco, D. Linten, W. Goes, T. Grasser, I. De Wolf, In *2020 IEEE International Reliability Physics Symposium (IRPS)*, IEEE, Dallas, TX, USA, **2020**, pp. 1–5.
[82] P. V. Sushko, S. Mukhopadhyay, A. S. Mysovsky, V. B. Sulimov, A. Taga, A. L. Shluger, *J. Phys. Condens. Matter* **2005**, *17*, S2115.
[83] S. Bonfanti, R. Guerra, C. Mondal, I. Procaccia, S. Zapperi, *Phys. Rev. E* **2019**, *100*, 060602.
[84] F. Bamer, S. S. Alshabab, A. Paul, F. Ebrahem, B. Markert, B. Stamm, *Scr. Mater.* **2021**, *205*, 114179.
[85] S. W. King, J. Brockman, M. French, M. Jaehnig, M. Kuhn, B. French, *J. Appl. Phys.* **2014**, *116*, 113703.
[86] S. P. Ogden, Y. Xu, K. B. Yeap, T. Shen, T.-M. Lu, J. L. Plawsky, *Microelectron. Reliab.* **2018**, *91*, 232.
[87] S. W. King, B. French, E. Mays, *J. Appl. Phys.* **2013**, *113*, 044109.
[88] M. A. Lampert, *Rep. Prog. Phys.* **1964**, *27*, 329.
[89] J. Frenkel, *Phys. Rev.* **1938**, *54*, 647.
[90] D. J. DiMaria, J. H. Stathis, *Appl. Phys. Lett.* **1997**, *71*, 3230.
[91] P. E. Nicollian, *Microelectron. Reliab.* **2008**, *48*, 1171.
[92] J. U. Bhanu, G. R. Babu, P. Thangadurai, *Mater. Sci. Semicond. Process.* **2019**, *89*, 85.
[93] V. Jousseaume, A. Zenasni, L. Favennec, G. Gerbaud, M. Bardet, J. P. Simon, A. Humbert, *J. Electrochem. Soc.* **2007**, *154*, G103.
[94] Y. Zheng, W. Zhu, T. F. Huang, S. Nemani, K. S. Yim, H. Amer, L. Q. Xia, H. M'Saad, *Proc. Adv. Met. Conf. 2003 AMC 2003 Mater. Res. Soc.* **2003**, *19*, 543.
[95] S. Jain, V. Zubkov, T. Nowak, A. Demos, J. C. Rocha, *Solid State Technol.* **2005**, *48*, 43.
[96] W. C. Oliver, G. M. Pharr, *J Mater Res* **2004**, *19*, 18.
[97] G. Kermouche, E. Barthel, D. Vandembroucq, Ph. Dubujet, *Acta Mater.* **2008**, *56*, 3222.

**Supporting Information**

# Evidence of Plasticity-Driven Conductivity Drop in an Ultra-Low-k Dielectric Organosilicate Glass

Morgan Rusinowicz*, Fabien Volpi, Guillaume Parry, Muriel Braccini, Chaymaa Boujrouf and Marc Verdier

## Meaning of the representative strain $\epsilon_{Rep}$

At each indentation step, the strain field underneath the indenter is fully determined by numerical modeling. Consequently, the maximum value of this strain field can be easily extracted, and the plot of the "current ratio" against this maximum strain at each step can be performed (**Figure S1**). However, this maximum strain is not the most relevant magnitude as it does not represent trustfully the strain field. A more physical approach is to modulate this magnitude by a numerical factor to obtain a representative scalar for this strain field. Any numerical factor would be acceptable and would not change the physical meaning of the present rationale. Among these factors, the 2.56 figure allows the slope of the "current ratio vs strain" curve to match the threshold strain of 1.72 % extracted independently.

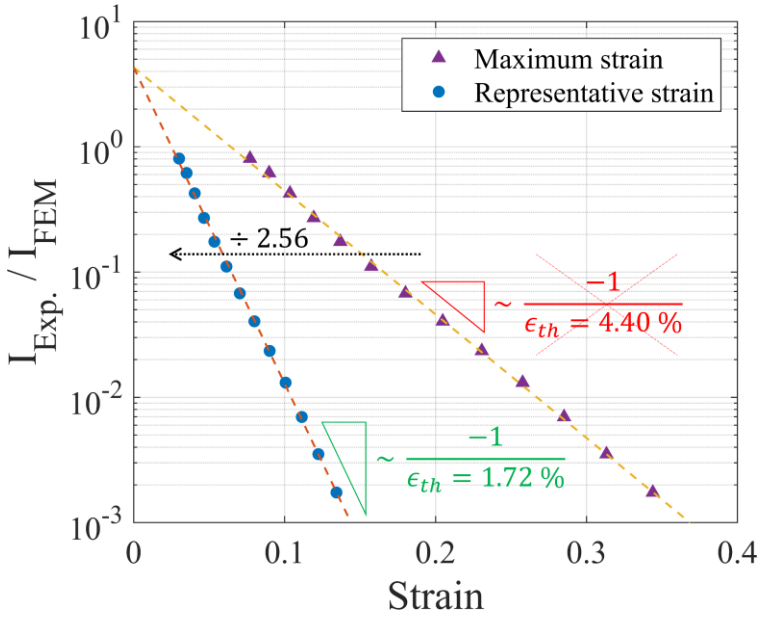


**Figure S1.** "Current ratio" vs the "maximum strain" (triangular markers) and the "representative strain" (circular markers).

**Choice of the strain measurement criterion**

**Figure S2**a,b,c,d represents the strain fields at 120 nm indentation depth of the maximum principal strain, the maximum principal elastic strain, the maximum principal plastic strain and the equivalent plastic strain respectively.

By comparing Figure S2a,b,c, it can be seen that the elastic strain level is ~10 % of the plastic strain and that the distribution of the maximum principal strain is largely driven by that of the maximum principal plastic strain. The impact of the elastic contribution can therefore be safely neglected.

By comparing Figure S2c,d, the FEM calculations indicate that the maximum principal plastic strain and the equivalent plastic strain distributions are similar and their levels are close.

Finally, Figure S2e shows that all approaches (excluding the elastic contribution alone) reproduce the experimental curve by adjusting the threshold strain by less than 10 %.

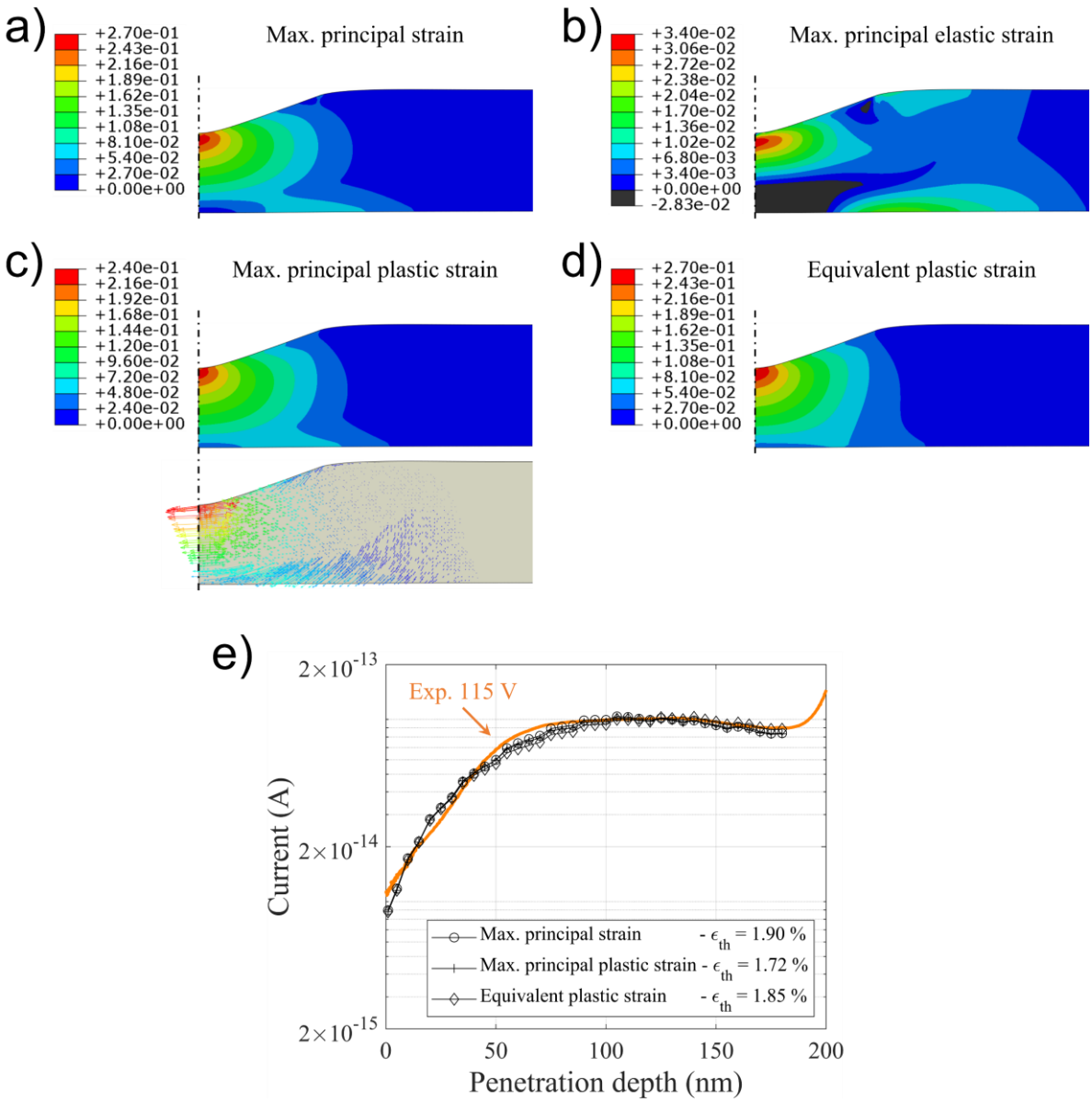


**Figure S2.** Strain fields at 120 nm indentation depth, representing a) the maximum principal strain, b) the maximum principal elastic strain, c) the maximum principal plastic strain and d) the equivalent plastic strain. e) Calculations from the strain-dependent Poole-Frenkel model considering different strain fields (maximum principal strain, maximum principal plastic strain, equivalent plastic strain), all matching the experimental current-depth curve at 115 V by adjusting the threshold strain by less than 10 %.

**Effect of trap density on the SiOCH band diagram: analytical modeling**

The SiOCH band diagram was calculated analytically by successive integrations of Gauss's law and of the relationship between potential and electric field:

$$\mathrm{div}(\boldsymbol{F}) = \frac{\rho}{\varepsilon_0 k} \quad \text{(S1)}$$

and

$$\boldsymbol{F} = -\mathbf{grad}(V) \quad \text{(S2)}$$

with $\boldsymbol{F}$ the electric field, $\rho$ the local charge density, $k$ the SiOCH relative permittivity and $V$ the electrostatic potential. The local charge density is controlled by the trap density $N_T$ :

$$\rho = eN_T \quad \text{(S3)}$$

The external bias $V_{App}$ is applied to the silicon substrate, while the reference bias 0 is applied to the diamond tip.

The system boundary conditions are the following:

- In 0: $V(0) = V_{App}$
- In $t$: $V(t) = 0$

Finally, one can obtain the following expressions:

$$F(x) = \frac{V_{App}}{t} + \frac{eN_T}{\varepsilon_0 k}\left(x - \frac{t}{2}\right) \quad \text{(S4)}$$

$$V(x) = V_{App} - F_0(N_T)\, x - \frac{eN_T}{2\varepsilon_0 k}\, x^2 \quad \text{(S5)}$$

with:

$$F_0(N_T) = \frac{V_{App}}{t} - \frac{eN_T}{\varepsilon_0 k}\, t \quad \text{(S6)}$$

The impact of the trap density on Poole-Frenkel emission should be calculated at the vicinity of the injecting electrode (silicon substrate). Several distances to this electrode were tested, leading to similar results. The results presented in the main body of the article were obtained at a distance where electrical screening fades: at the Debye length $\lambda_D$.

$$\lambda_D = \sqrt{\frac{\varepsilon_0 k k_B T}{e^2 N_T}} \quad \text{(S7)}$$

Finally, the increment in Poole-Frenkel barrier lowering due to the traps was calculated from the difference between the actual barrier lowering (with space charge) and the original Poole-Frenkel barrier lowering (without space charge):

$$\Delta\phi_{SC} = \sqrt{\frac{eF(\lambda_D)}{\pi\varepsilon}} - e\sqrt{\frac{eV_{App}/t}{\pi\varepsilon}}\, e \quad \text{(S8)}$$

**Ohmic conduction at low electric fields**

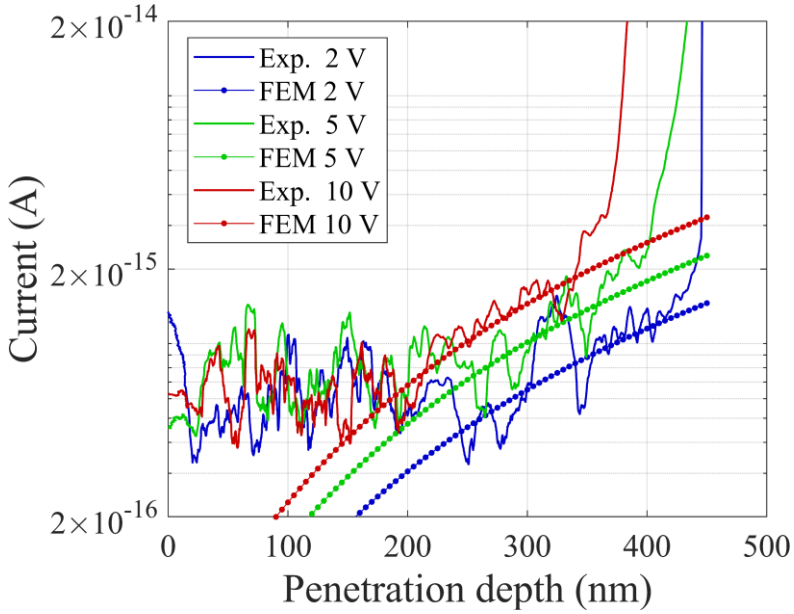


**Figure S3.** Comparison of the experimental and numerical current-depth curves for voltages of 2, 5 and 10 V. The FEM curves come from the "strain-dependent PF + Ohm" model with the properties given in this article, but here they are fully driven by the ohmic regime.

**Numerical model description**

Numerical calculations were carried out by the Finite Element Method (FEM) using the ABAQUS® software within the framework of a 2D axisymmetric model. The model is composed of three parts, consisting of deformable bodies:

- The substrate. It has a cylindrical shape with a radius and height of 10 µm. These dimensions are chosen to be sufficiently large compared to the maximum indentation depth (200 nm) to avoid any interaction of the stress/strain fields generated in the material with the outer boundary of the sample (and also so that the electric fields do not interact with the edges).
- The film. It has a thickness of 330 nm and a radius equal to that of the substrate (10 µm). It is fully tied to the substrate (i.e., nodes of the film and the substrate are merged along the film/substrate interface), which ensures perfect continuity of the mechanical and electric fields between these two parts.
- The indenter. It has a cono-spherical geometry, chosen to match the profile of the experimentally used Berkovich tip (i.e. its area function relating the section of the tip to the distance from its apex). Its height is 10 µm, chosen for the same reasons as for the substrate.

The goal of the simulations is to reproduce electrical-nanoindentation tests in order to capture both the mechanical and electric fields in the SiOCH film (stress/strain and current density/electric field distributions). For this, they are divided into three steps in which the bottom surface of the substrate is always mechanically embedded and the top surface of the tip is at zero voltage. In the first step, a small downward displacement of one nanometer is applied to the upper surface of the tip in order to bring it into contact with the film surface. In the second step, a voltage is applied incrementally to the bottom surface of the substrate until the desired voltage for the electrical-indentation test is reached. Finally, in the third step, a displacement of the tip on the film surface continues to be applied incrementally to a maximum depth of 200 nm, while maintaining the desired voltage constant. The elements available in the ABAQUS® software do not allow the mechanical and electrical physics to be coupled in a 2D axisymmetric framework. A coupled thermal-stress analysis is therefore performed, in which the mechanical and thermal equations are solved simultaneously. The idea is to make an analogy between heat transfer and electrical conduction in a stationary state. Throughout this study, the temperature is thus assimilated to the electric potential and the heat flux density is assimilated to the electric current density.

The calculations are carried out in the framework of large displacements. A steady-state coupled temperature-displacement analysis is performed using the ABAQUS®/Standard solver. “Temperatures” (i.e. values of the potential) are integrated using a backward-difference scheme, and the nonlinear coupled system is solved using Newton's method.

The indenter/film mechanical contact is defined as “hard” and “frictionless”, which means that the penetration of the film surface into the tip surface is minimized. Concerning the electrical contact, the conduction is defined as “infinite” (“conductance” of $10^{23}$ $\Omega^{-1}$ $cm^{-2}$) when the distance between the surfaces of the indenter and the film is zero (“clearance” of 0 nm) and the conduction is specified as nil when the clearance is 1 nm or more.

The elements used to mesh the three parts are 3-node axisymmetric linear interpolation for displacement and temperature elements (CAX3T in ABAQUS®) with a size of 10 nm in the film and near the indenter/film and film/substrate interfaces. A convergence study (not shown) was carried out in order to check that the mesh was fine enough so that the results obtained were independent of the element size.

The post-processing consists of calculating mainly two quantities during the indentation: the mechanical force and the electrical current. The reaction force of the substrate to the displacement of the indenter (boundary condition) is determined by summing the vertical nodal

reaction force components of the bottom surface of the substrate. The current induced by the electric potential bias (boundary condition) corresponds to the current flux crossing the film/indenter interface. It is therefore possible to plot both "force – displacement" mechanical loading curves and "current – displacement" electrical curves at fixed voltage, as in the case of an experimental electrical-nanoindentation test.

A schematic summarizing the model parts, dimensions, boundary conditions and mesh is shown in **Figure S4**.

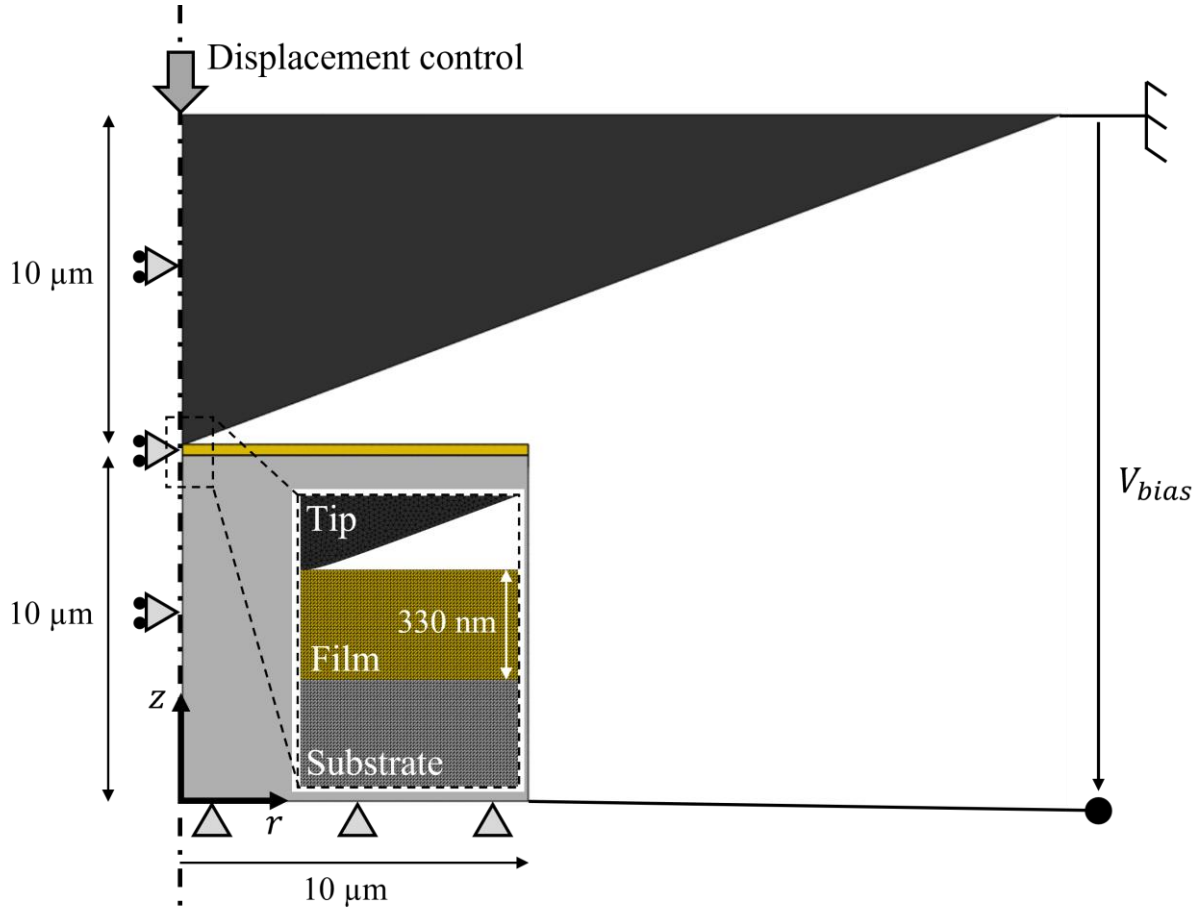


**Figure S4.** Numerical model for the FEM simulations.

Concerning the mechanical behavior of the materials, the boron-doped diamond indenter and the (001)-oriented silicon substrate are assumed to be linear elastic isotropic. The Young's modulus and Poisson's ratio of these materials are well known and were fixed in the numerical model. The film is assumed to be elastic-plastic since residual imprints were measured by AFM even before the mechanical cracking associated with the first pop-in (see section 2.2 of this article), which is the signature of a non-reversible deformation. Its elastic regime is described by an linear elastic isotropic law with a Poisson's ratio fixed at 0.2.[1] As SiOCH undergoes non-

reversible deformation under shear during mechanical loading, as well as nanoporosity densification under the effect of hydrostatic pressure, a yield criterion taking into account the effect of hydrostatic pressure is needed in order to model its plastic behavior properly. This is why a Drucker-Prager yield criterion was chosen. In the ABAQUS® software, we chose a linear Drucker-Prager law, with the yield surface defined as:

$$\sigma_{eq} - p\tan(\beta) - d = 0 \quad \text{(S9)}$$

with $p$ the hydrostatic pressure:

$$p = -\frac{1}{3}\,\mathrm{trace}(\boldsymbol{\sigma}) \quad \text{(S10)}$$

and $\sigma_{eq}$ the Mises equivalent stress:

$$\sigma_{eq} = \sqrt{\frac{3}{2}(\mathbf{S} : \mathbf{S})} \quad \text{(S11)}$$

where **S** is the stress deviator, defined as:

$$\mathbf{S} = \boldsymbol{\sigma} + p\,\mathbf{I} \quad \text{(S12)}$$

$\beta$ is the slope of the linear yield surface in the $p$–$\sigma_{eq}$ stress plane (also called the internal friction angle of the material).

Finally, $d$ is called the cohesion parameter, defined as:

$$d = \left(1 - \frac{1}{3}\tan(\beta)\right)\sigma_c \quad \text{(S13)}$$

where $\sigma_c$ is the uniaxial compression yield stress.

Thanks to an inverse analysis methodology based on the experimental loading curves the following film properties were determined: its Young's modulus $E$, its friction angle $\beta$ and its uniaxial compression yield stress $\sigma_c$.

First, the friction angle was determined by a method proposed by [2] which relates $\beta$ to the irreversible work fraction $W_{irr}/W_{tot}$ measured from the area under the experimental loading/unloading curves. Thus, an angle of 30 ° was identified.

The other two parameters ($E$ and $\sigma_c$) were determined by fitting the simulated load versus penetration curve to the experimental one. However, if we consider $\sigma_c$ to be independent of the plastic strain (i.e. plasticity without hardening), two problems seem to appear after the inverse analysis:

- The Young's modulus is out of the range estimated in the literature for a SiOCH film of a few hundred nanometers thickness with ~ 25% of nanoporosities ($E$ ~ 8 GPa according to [1]).

- The value of the uniaxial compression yield stress does not allow the material to enter its plastic domain from a few tens of nanometers of indentation as experimentally observed by AFM (see section 2.2 of this article).

This is explained by the phenomenon of densification-induced hydrostatic hardening, which is known for amorphous silica.[3,4] In our simulations, this effect is incorporated by using a linear hardening law relating the uniaxial compression stress $\sigma_c$ to the equivalent plastic strain $\epsilon_{eq}^{pl}$, such that:

$$\sigma_c = \sigma_{c0} + K\,\epsilon_{eq}^{pl} \tag{S14}$$

with $\sigma_{c0}$ the initial uniaxial compression yield stress and $K$ the hardening modulus.

In order for the material to undergo non-reversible deformations from the first tens of nanometers of indentation, $\sigma_{c0}$ was arbitrarily set at a low value of 100 MPa. Moreover, it was noticed that for a Young's modulus varying around 8 GPa, the value of the hardening modulus also varied around this value. It was therefore assumed that these moduli were equal. By adjusting them until the difference between the experimental and simulated load-depth curves is minimized, we obtained $E = K = 7.6$ GPa.

In order to understand the magnitude of $K$, it is worth noting that the mechanisms governing plastic deformation in amorphous materials are quite different from those arising in metallic solids. In the latter case, the mechanisms are well known and rely on the pinning of dislocations, or the interaction between dislocation systems, resulting in shear-hardening slopes two orders of magnitude lower than the elastic modulus. In the case of amorphous silica, $K$ and $E$ have been found to be of the same order,[3] so it is not surprising to reach a similar conclusion in our case.

Concerning the electrical behavior of the materials, that of the boron-doped diamond indenter and the (001)-oriented silicon substrate is assumed to be ohmic, while that of the SiOCH film is what we seek to identify. As stated in section 4 of this article, the choice of constitutive laws and electrical properties of these two materials does not change the results because the SiOCH film is more resistive by several orders of magnitude. Electrical transport is therefore limited by the film and not by the indenter or the substrate.

**Table S1** gives all the material properties implemented in the numerical model.

**Table S1.** Material properties used in FEM simulations.

| Part / Material | Elastic properties | | Plastic properties | | | Electric properties |
|---|---|---|---|---|---|---|
| | $E$ [GPa] | $v$ [-] | $\beta$ [°] | $\sigma_{c0}$ [MPa] | $K$ [GPa] | $\sigma_{Ohm}$ [$\Omega^{-1}$ cm$^{-1}$] |
| Indenter / Boron-doped diamond | 1140 | 0.07 | - | - | - | 0.1 |
| Substrate / (001)-oriented silicon | 130 | 0.28 | - | - | - | 0.1 |
| Film / Nanoporous SiOCH | 7.6 | 0.2 | 30 | 100 | 7.6 | In this article |

By default, the steady state conduction law in ABAQUS® is Fourier's law, i.e. Ohm's law with our thermal-electrical analogy. In order to change this constitutive law in the SiOCH film, the UMATHT subroutine was used. In this subroutine, two relations have to be defined: the heat flux density vector (current density vector) with respect to the spatial gradients of temperature (spatial gradients of electric potential) and the variation of this vector with respect to the gradients. Concerning the dependence of the conduction law on the mechanical strain, the USDFLD subroutine was also used. It allowed us to use the strain (defined at the element integration points) as a field variable, to store it as a solution-dependent state variable, and finally to pass it into the UMATHT subroutine to integrate it into the conduction law.

## References


[1] W. Zhou, S. Bailey, R. Sooryakumar, S. King, G. Xu, E. Mays, C. Ege, J. Bielefeld, *J. Appl. Phys.* **2011**, *110*, 043520.

[2] L. Charleux, *PhD thesis*, Grenoble INP university France, December, **2006**.

[3] G. Kermouche, E. Barthel, D. Vandembroucq, Ph. Dubujet, *Acta Mater.* **2008**, *56*, 3222.

[4] A. Perriot, D. Vandembroucq, E. Barthel, V. Martinez, L. Grosvalet, Ch. Martinet, B. Champagnon, *J. Am. Ceram. Soc.* **2006**, *89*, 596.

**Table of Contents**

**Evidence of Plasticity-Driven Conductivity Drop in an Ultra-Low-k Dielectric Organosilicate Glass**

Morgan Rusinowicz*, Fabien Volpi, Guillaume Parry, Muriel Braccini, Chaymaa Boujrouf and Marc Verdier

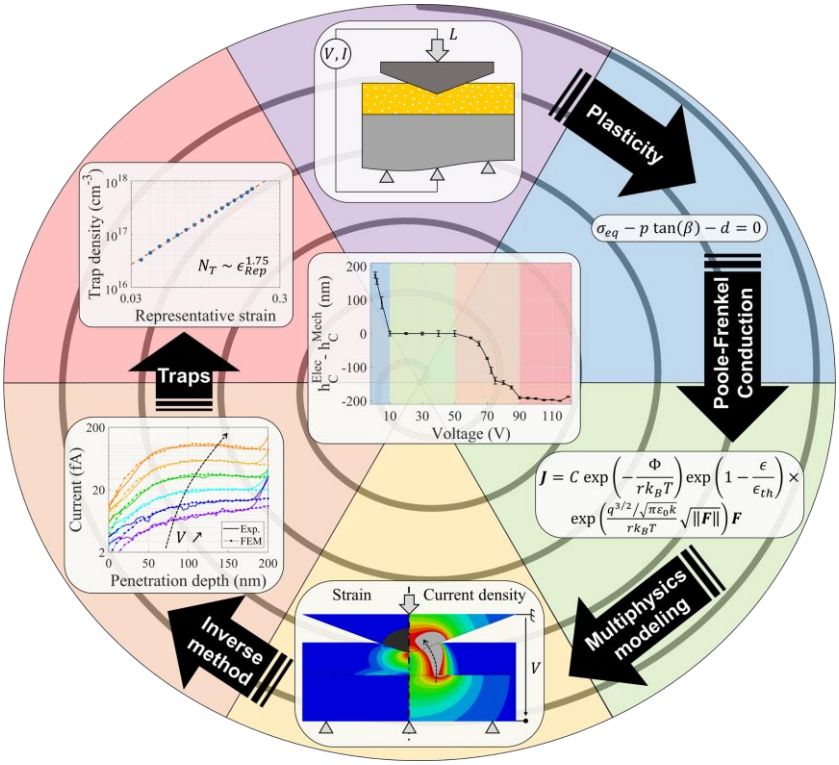


The interplay between structural defects, induced by plastic deformation, and electrical conduction in an ultra-low-permittivity organosilicate glass is fully described. Thanks to an approach coupling in situ experiments with numerical/analytical modeling, a conductivity drop under high mechanical stresses can be fully explained. This new understanding of the mechanical/electrical coupling in dielectrics opens promising insights into reliability issues of advanced devices.